





A quantitative model predicts how m⁶A reshapes the kinetic landscape of nucleic acid hybridization and conformational transitions

Bei Liu ¹, Honglue Shi ², Atul Rangadurai¹, Felix Nussbaumer³, Chia-Chieh Chu^{1,5}, Kevin Andreas Erharder³, David A. Case⁴, Christoph Kreutz ³ & Hashim M. Al-Hashimi ^{1,2}✉

*N*⁶-methyladenosine (m⁶A) is a post-transcriptional modification that controls gene expression by recruiting proteins to RNA sites. The modification also slows biochemical processes through mechanisms that are not understood. Using temperature-dependent (20°C–65°C) NMR relaxation dispersion, we show that m⁶A pairs with uridine with the methylamino group in the *anti* conformation to form a Watson-Crick base pair that transiently exchanges on the millisecond timescale with a singly hydrogen-bonded low-populated (1%) mismatch-like conformation in which the methylamino group is *syn*. This ability to rapidly interchange between Watson-Crick or mismatch-like forms, combined with different *syn:anti* isomer preferences when paired (~1:100) versus unpaired (~10:1), explains how m⁶A robustly slows duplex annealing without affecting melting at elevated temperatures via two pathways in which isomerization occurs before or after duplex annealing. Our model quantitatively predicts how m⁶A reshapes the kinetic landscape of nucleic acid hybridization and conformational transitions, and provides an explanation for why the modification robustly slows diverse cellular processes.

¹Department of Biochemistry, Duke University School of Medicine, Durham, NC, USA. ²Department of Chemistry, Duke University, Durham, NC, USA.

³Institute of Organic Chemistry and Center for Molecular Biosciences Innsbruck (CMBI), University of Innsbruck, Innsbruck, Austria. ⁴Department of Chemistry and Chemical Biology, Rutgers University, Piscataway, NJ, USA. ⁵Present address: Department of Chemistry, University of Chicago, Chicago, IL, USA. ✉email: hashim.al.hashimi@duke.edu

N⁶-methyladenosine (m⁶A) (Fig. 1a) is an abundant RNA modification^{1,2} that helps control gene expression in a variety of physiological processes including cellular differentiation, stress response, viral infection, and cancer progression^{3–5}. m⁶A is also the most prevalent form of DNA methylation in prokaryotes where it is used to distinguish benign host DNA from potentially pathogenic nonhost DNA⁶. Although under debate⁷, there is also evidence for m⁶A in mammalian DNA where it is proposed to play roles in transcription suppression and gene silencing^{8,9}.

In RNAs, m⁶A is thought to primarily function by recruiting proteins to specific modified sites (reviewed in refs. 3–5). However, there is also growing evidence that the modification can impact a range of biochemical processes by changing the behavior of the methylated RNAs^{10,11}. For example, by destabilizing canonical double-stranded RNA (dsRNA)¹², m⁶A has been shown to promote the binding of proteins to single-stranded regions of RNAs (ssRNAs)¹⁰. The modification has also been shown to slow biochemical processes that involve base pairing. For example, in messenger RNAs (mRNAs), m⁶A delays transfer RNA (tRNA) selection and reduces the translation efficiency in vitro¹³ and in vivo¹⁴ by 3–15-fold. In mRNA introns, m⁶A slows splicing and promotes alternative splicing in vivo¹⁵. Additionally, m⁶A reduces the rate of NTP incorporation during DNA replication¹⁶ and reverse transcription¹⁷ in vitro by 2–13-fold.

Recently, we developed and validated a nuclear magnetic resonance (NMR) relaxation–dispersion (RD)^{18–20}-based method to measure the hybridization kinetics in DNA and RNA duplexes²¹. Using this approach, we showed that m⁶A preferentially slows the apparent rate of RNA duplex annealing by ~5–10-fold while having little effect on the apparent rate of duplex melting²¹ (Fig. 1b). This impact of m⁶A on hybridization kinetics stands in contrast to mismatches that slow the rate of duplex annealing and also substantially increase the rate of duplex melting by up to ~100-fold^{22–24}. How m⁶A selectively slows duplex annealing remains unknown. The comparable m⁶A-induced slowdown observed for duplex annealing and a variety of biochemical processes indicates that a common mechanism might be at play^{13,16,17}.

It has been known for many decades that the methylamino group of the m⁶A nucleobase can form two rotational isomers that interconvert on the millisecond timescale^{25,26} (Fig. 1a). The preferred *syn* isomer^{12,25,26} cannot form a canonical Watson–Crick base pair (bp) with uridine as the methyl group impedes one of the hydrogen bonds (H-bonds) (Fig. 1a). Rather, when paired with uridine, the methylamino group rotates into the energetically disfavored *anti* isomer and forms a canonical m⁶A–U Watson–Crick bp that retains both (A)N1...H-N3(U) and (A)N6...H-O4(U) H-bonds (Fig. 1a). As isomerization is energetically disfavored, it has been proposed to explain how m⁶A destabilizes dsRNA via the so-called “spring-loading”¹² mechanism despite forming a canonical Watson–Crick m⁶A–U bp.

Kinetic mechanisms involving binding and conformational change can occur via pathways wherein the conformational change occurs prior to or post binding²⁷. We, therefore, hypothesized that m⁶A could slow hybridization via at least two pathways in which isomerization of the methylamino group occurs either before or following duplex formation (Fig. 1c). In the conformational selection (CS) pathway, hybridization proceeds via an unpaired intermediate (ssRNA^{anti}) with m⁶A in the energetically disfavored *anti* conformation (Fig. 1c). In the induced-fit (IF) pathway, the more populated ssRNA^{syn} species with m⁶A in the *syn* conformation initially hybridizes to form a double-stranded intermediate (dsRNA^{syn}) that entails the loss of at least one Watson–Crick H-bond between m⁶A and the partner uridine (Fig. 1a). This is then followed by isomerization to form the Watson–Crick bp (dsRNA^{anti}) with m⁶A in the *anti* conformation (Fig. 1c). To date, there has been no evidence for the dsRNA^{syn} intermediate.

Here, using NMR RD, we show that m⁶A with the methylamino group in the *anti* conformation forms a Watson–Crick bp with uridine that transiently exchanges on the millisecond timescale with an unusual singly hydrogen-bonded, low-populated (1%), and mismatch-like conformation through isomerization of the methylamino group to the *syn* conformation. This ability to rapidly interchange between Watson–Crick or mismatch forms, combined with different *syn:anti* isomers preferences when paired versus unpaired, explains how m⁶A robustly and selectively slows

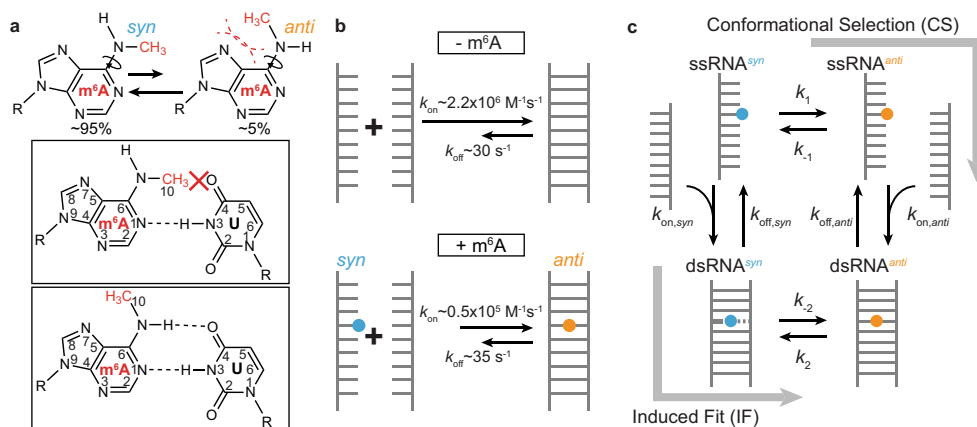


Fig. 1 The *syn* and *anti* isomers of m⁶A. **a** The m⁶A nucleobase shows a 20:1 preference for the *syn* isomer due to unfavorable steric interactions (shown in dashed red lines) in the *anti* isomer^{12, 25}. In a duplex, the *syn* isomer impedes Watson–Crick pairing, and the *anti* isomer becomes the dominant form. **b** Apparent annealing (k_{on}) and melting (k_{off}) rate constants for unmethylated (–m⁶A) and methylated (+m⁶A) dsRNA. Rate constants shown were obtained from CEST measurements on dsGGACU with and without m⁶A at $T = 65 \text{ }^\circ\text{C}$ ²¹. **c** Schematic of the general four-state CS + IF model. k_1 and k_{-1} are the forward and backward rate constants for methylamino isomerization in ssRNA, respectively; k_2 and k_{-2} are the forward and backward rate constants for methylamino isomerization in dsRNA, respectively; $k_{on,anti}$ and $k_{off,anti}$ are the annealing and melting rate constants, respectively, when m⁶A adopts *anti* conformation in both ssRNA and dsRNA; $k_{on,syn}$ and $k_{off,syn}$ are the annealing and melting rate constants, respectively when m⁶A adopts *syn* conformation in both ssRNA and dsRNA.

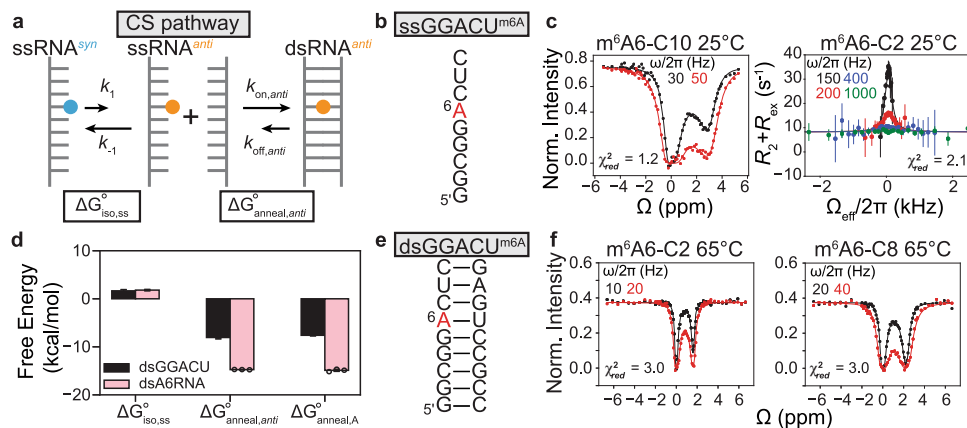


Fig. 2 Testing a conformational selection kinetic model for m^6A hybridization. **a** The CS pathway. $\Delta G_{\text{iso,ss}}^{\circ}$ is the free energy of methylamino isomerization in ssRNA. $\Delta G_{\text{anneal,anti}}^{\circ}$ is the free energy of annealing the methylated ssRNA when m^6A is *anti*. **b** ssGGACU sequence with the m^6A site is highlighted in red. **c** ^{13}C CEST profile for $m^6A6\text{-C}10$ and off-resonance ^{13}C $R_{1\rho}$ RD profile for $m^6A6\text{-C}2$ in ssGGACU $^{m^6A}$. **d** Free energy decomposition (see “Methods”) of the CS pathway for dsGGACU $^{m^6A}$ at $T = 65^\circ\text{C}$ and dsA6RNA $^{m^6A}$ (Supplementary Fig. 1) at $T = 20^\circ\text{C}$. $\Delta G_{\text{anneal,A}}^{\circ}$ is the free energy of annealing unmethylated ssRNA and the value for dsGGACU was obtained from a prior study using RD measurements²¹, and for dsA6RNA was measured using UV melting experiments (Supplementary Table 4). Data for $\Delta G_{\text{iso,ss}}^{\circ}$ were presented as mean values ± 1 s.d. from Monte Carlo simulations for one RD measurement. Data for $\Delta G_{\text{anneal,A}}^{\circ}$ were presented as mean values ± 1 s.d. from $n = 3$ independent UV measurements. The errors for $\Delta G_{\text{anneal,anti}}^{\circ}$ were propagated from $\Delta G_{\text{iso,ss}}^{\circ}$ and $\Delta G_{\text{anneal,A}}^{\circ}$. **e** The dsGGACU $^{m^6A}$ duplex with the m^6A site highlighted in red. **f** ^{13}C CEST profiles for $m^6A6\text{-C}2$ and C8 in dsGGACU $^{m^6A}$ at $T = 65^\circ\text{C}$ (data obtained from a prior study²¹). Solid lines in panels (**c**, **f**) denote a two-state and constrained three-state fit to the CS pathway, using Bloch–McConnell equations as described in “Methods”. Buffer conditions for NMR experiments are described in “Methods”. RF field powers used for CEST and spin-lock powers used for $R_{1\rho}$ are color-coded. Data for CEST profiles (**c**, **f**) were presented as mean values ± 1 s.d. (smaller than data points) from $n = 3$ independent measurements of peak intensities at zero relaxation delay (see “Methods”). Data for the $R_{1\rho}$ profile in panel (**c**) were presented as mean values ± 1 s.d. from Monte Carlo simulations for one measurement as described in “Methods”. Source data for panel (**d**) are provided in the Source Data file.

duplex annealing without affecting melting via two pathways in which isomerization occurs before or after duplex annealing. We develop a model that quantitatively predicts how m^6A reshapes the kinetic landscape of nucleic acid hybridization, and that could explain why the modification robustly slows a variety of cellular processes. The model also predicts that m^6A more substantially slows fast intramolecular RNA conformational transitions, and this prediction was verified experimentally by using NMR.

Results

Kinetics of m^6A methylamino isomerization in ssRNA. The ssRNA anti which is the intermediate along the CS pathway has been extensively characterized in the past, whereas there is no evidence for the dsRNA syn IF intermediate. We therefore initially examined whether the CS pathway alone could explain how and why m^6A reduces the rate of duplex annealing while not affecting the melting rate. We developed a CS model which assumes that the minor *anti* isomer of m^6A hybridizes with apparent annealing (k_{on}) and melting (k_{off}) rate constants similar to those of the unmethylated RNA. This assumption is reasonable given that like unmethylated adenine, the *anti* isomer forms a canonical $m^6A\text{-U}$ Watson–Crick bp when paired with uridine^{11,12,25,26}. Since the *syn* isomer is incapable of Watson–Crick pairing with uridine, the model assumes that hybridization only proceeds via annealing of the single-strand containing the minor *anti* isomer (ssRNA anti) through a CS-type pathway^{27,28} (Fig. 2a). The apparent k_{on} would then be reduced relative to the unmethylated RNA because the methylamino group has to rotate from the major *syn* to the minor *anti* isomer prior to hybridization (Fig. 2a). However, because *anti* is the preferred isomer in the canonical duplex, and because hybridization is rate-limiting under our experimental conditions (see below), the apparent k_{off} would remain equivalent to that of the unmethylated duplex.

To test this CS model, we first used NMR RD to measure the isomerization kinetics in a ssRNA containing the most abundant m^6A consensus sequence^{1,2} in eukaryotic mRNAs (ssGGACU $^{m^6A}$; Fig. 2b). This was important given that prior kinetic measurements of isomerization were performed on the m^6A nucleobase dissolved in organic solvents and the kinetics may differ in ssRNA under aqueous conditions²⁵.

To enable the RD measurements, we used organic synthesis (see “Methods”) to incorporate m^6A ^{13}C labeled at the base C2 and C8, or methyl C10 carbons (Supplementary Fig. 1) into ssGGACU. We then performed NMR chemical exchange saturation transfer (CEST)^{29–31} and off-resonance spin relaxation in the rotating frame ($R_{1\rho}$) experiments^{18–20} to measure the isomerization kinetics. NMR RD experiments can be used to characterize conformational exchange between a dominant ground-state (GS) and short-lived low-populated “excited-state” (ES). The $R_{1\rho}$ experiment measures the line-broadening contribution (R_{ex}) to the transverse relaxation rate (R_2) during a relaxation period in which a continuous radiofrequency (RF) field is applied with variable power (ω_{SL}) and frequency (ω_{RF}). The RF field reduces the R_{ex} contribution in a manner dependent on ω_{SL} and ω_{RF} and the exchange parameters of interest (see below). The RD profiles are typically displayed by plotting the measured $R_2 + R_{\text{ex}}$ as a function of ω_{SL} and ω_{RF} . For detectable exchange, a peak is observed centered at the difference between the chemical shift of the GS and ES ($-\Delta\omega$, assuming $\omega_{\text{GS}} = 0$ and $\omega_{\text{ES}} = \Delta\omega$). The CEST experiment measures the impact of conformational exchange on longitudinal GS magnetization during a relaxation period following application of a continuous RF field with variable power (ω_{SL}) and frequency (ω_{RF}). When applied on resonance with the ES, the RF field saturates the ES magnetization, and this saturation can be transferred via conformational exchange to the GS. This typically results in a reduced signal

intensity for the GS and a minor dip centered at $\omega_{ES} = \Delta\omega$ when the RF is on resonance with ES. A major dip is also observed centered at $\omega_{GS} = 0$ when the RF field is on resonance with the GS. The dependencies of $R_2 + R_{ex}$ ($R_{1\rho}$) or the GS signal intensity (CEST) on ω_{SL} and ω_{RF} can be fit to the Bloch–McConnell (B–M) equations³² describing N-site exchange to determine exchange parameters of interest (see below). Together, $R_{1\rho}$ and CEST, which are optimized for different nuclei and exchange kinetics, allowed robust characterization of chemical exchange between the major GS *syn* methylamino and the low-populated and short-lived ES³³ *anti* methylamino isomer in unpaired m⁶A.

Shown in Fig. 2c on the left is the CEST profile recorded for the m⁶A-C10 methyl carbon in ssGGACU^{m⁶A} as a function of RF. As is typical for CEST profiles, a major dip is observed when the RF field is on-resonance with the GS chemical shift at $\Delta\omega = 0$. In addition, a minor dip was observed indicative of conformational exchange with a sparsely populated ES. The dip was observed at a chemical shift $\Delta\omega_{C10} = \omega_{ES} - \omega_{GS} = 3$ p.p.m., which was in good agreement with the value predicted for the *anti* isomer ($\Delta\omega_{C10} = 3$ –5 p.p.m.) using density functional theory (DFT) calculations³⁴ (see “Methods”). Shown in Fig. 2c on the right is the $R_{1\rho}$ profile measured for m⁶A-C2 in ssGGACU^{m⁶A} as a function of RF field. A peak was observed at $-\Delta\omega_{C2} = 0.6$ p.p.m. indicative of conformational exchange. A similar C2 RD was observed in methylated but not unmethylated AMP, as expected if the RD is reporting on isomerization (Supplementary Fig. 2a).

Based on a two-state fit of the m⁶A-C10 and m⁶A-C2 RD data (Fig. 2c), the population of the ssRNA^{*anti*} isomer in ssGGACU^{m⁶A} was ~9% and the exchange rate for isomerization ($k_{ex} = k_1 + k_{-1}$, where k_1 and k_{-1} are the forward and backward rate constants, respectively) was ~600 s⁻¹ at $T = 25$ °C (Supplementary Table 1). The population was ~2-fold higher than the value measured in the nucleobase in organic solvent (Fig. 1a)²⁵ while the exchange rate was ~20-fold faster, and in better agreement with values reported recently for ssDNA³⁵ (at $T = 45$ °C; Supplementary Table 1). Similar *syn*–*anti* isomerization kinetics were obtained for another different sequence (Supplementary Fig. 2b).

m⁶A(*anti*)–U and A–U have similar thermodynamic stabilities in dsRNA. Before testing whether the CS model can predict the hybridization kinetics of methylated duplexes, we tested a thermodynamic prediction made by our model, namely that the energetics of annealing a single-strand containing the *anti* isomer of m⁶A should be similar to the energetics of annealing the unmethylated control. In this scenario, m⁶A destabilizes a duplex¹² primarily due to the conformational penalty ($\Delta G_{iso,ss}^\circ$) accompanying *syn* to *anti* isomerization in the ssRNA, which we have measured here for ssGGACU^{m⁶A} using NMR RD.

To test this prediction, we decomposed (Fig. 2a) the overall annealing energetics ($\Delta G_{anneal,m^6A}^\circ = -6.5 \pm 0.1$ kcal/mol) of methylated dsGGACU^{m⁶A} (Fig. 2e) measured previously using melting experiments²¹ into the sum of $\Delta G_{iso,ss}^\circ = 1.6 \pm 0.2$ kcal/mol plus the desired annealing energetics ($\Delta G_{anneal,anti}^\circ$) of m⁶A when it adopts the *anti* isomer,

$$\Delta G_{anneal,m^6A}^\circ = \Delta G_{iso,ss}^\circ + \Delta G_{anneal,anti}^\circ$$

Indeed, we find that $\Delta G_{anneal,anti}^\circ = -8.1 \pm 0.2$ kcal/mol is similar to that measured for the unmethylated RNA $\Delta G_{anneal,A}^\circ = -7.6 \pm 0.1$ kcal/mol, with the methyl group being only slightly stabilizing within error by 0.5 ± 0.2 kcal/mol. A similar result was obtained for a different duplex (Fig. 2d) and a similar conclusion was also reached previously using the isomerization energetics measured in the nucleobase^{25,26}.

Therefore, with respect to the thermodynamics of annealing canonical duplexes, m⁶A in the *anti* isomer behaves similarly (within <0.5 kcal/mol) to unmethylated adenine and m⁶A primarily destabilizes dsRNA due to the conformational penalty accompanying isomerization, consistent with the previously proposed “spring-loading” mechanism¹². Consistent with this interpretation, RD measurements on the m⁶A monomer reveal that 3 mM Mg²⁺ stabilizes the *anti* relative to *syn* isomer by ~0.5 kcal/mol³⁶, and correspondingly, the destabilizing effects of m⁶A on RNA duplexes is reduced by ~0.2 kcal/mol in the presence of 3 mM Mg²⁺ relative to the absence of Mg²⁺ (Supplementary Table 1).

Testing the CS kinetic model. Next, we tested whether the CS kinetic model could explain the impact of m⁶A on the hybridization kinetics of the dsGGACU^{m⁶A} RNA measured recently using NMR RD²¹. These experiments were performed at $T = 65$ °C under conditions in which the duplex was the GS, and the ssRNA comprising two species in rapid equilibrium (ssRNA^{*syn*} \rightleftharpoons ssRNA^{*anti*}) was the ES with a population of ~25%. The CEST experiments were performed at high temperatures because at 37 °C, the ssRNA is too lowly populated (<0.1%) and the hybridization is too slow (<50 s⁻¹) to be effectively characterized by RD. Based on a two-state fit (dsRNA \rightleftharpoons ssRNA) of the m⁶A6-C2 and m⁶A6-C8 RD data (Supplementary Fig. 3a), m⁶A reduced the apparent rate of dsGGACU^{m⁶A} annealing (k_{on,m^6A}^{app}) relative to the unmethylated control (k_{on}) by 5-fold while having little impact on the melting rate ($k_{off,m^6A}^{app} \approx k_{off}$)²¹.

We used the three-state CS model to simulate the m⁶A6-C8 and m⁶A6-C2 RD profiles measured for the methylated dsGGACU^{m⁶A} duplex. The exchange parameters for the first isomerization step (ssRNA^{*syn*} \rightleftharpoons ssRNA^{*anti*}) were fixed to the values determined independently from RD measurements on ssGGACU^{m⁶A} (Supplementary Fig. 2c). $k_{off,anti}$ was assumed to be equal to k_{off} measured for the unmethylated dsGGACU. This assumption is reasonable considering that hybridization is rate-limiting under our experimental conditions, and given the similarity between the experimentally measured k_{off} for methylated and unmethylated duplexes²¹. The value of $k_{on,anti}$ was slightly adjusted relative to k_{on} of the unmethylated control ($k_{on,anti} \approx 2 \times k_{on}$) to take into account small differences in their annealing energetics (Fig. 2a). The remaining NMR exchange parameters ($\Delta\omega$, R_1 , and R_2 of GS and two ESs) for the hybridization and isomerization steps were fixed to the values obtained from the two-state fit of the RD data measured for dsGGACU^{m⁶A} and ssGGACU^{m⁶A} (see “Methods”).

Interestingly, this simulation with no adjustable parameters satisfactorily reproduced the RD data with $\chi_{red}^2 = 6.8$. This can be compared with $\chi_{red}^2 = 3.3$ (Supplementary Fig. 3a) obtained from a two-state fit of the RD data with six adjustable parameters. As a negative control, the agreement deteriorated considerably ($\chi_{red}^2 = 51.5$) (Supplementary Fig. 3b) when decreasing the exchange rate by 20-fold to mimic values observed for the nucleobase in organic solvents²⁵. A constrained three-state fit to the RD data using the CS model in which the exchange parameters were allowed to vary within experimental error by 1 s.d., and in which the ratio (but not absolute magnitude) of $k_{on,anti}$ and $k_{off,anti}$ was constrained to preserve the free energy of the hybridization step improved the agreement to $\chi_{red}^2 = 3.0$ (see “Methods” and Fig. 2f) and yielded $k_{on,anti} \approx 2 \times k_{on}$ and $k_{off,anti} \approx k_{off}$ (Supplementary Table 2). Therefore, even when it comes to hybridization kinetics, m⁶A in the *anti* isomer behaves similarly to unmethylated adenine.

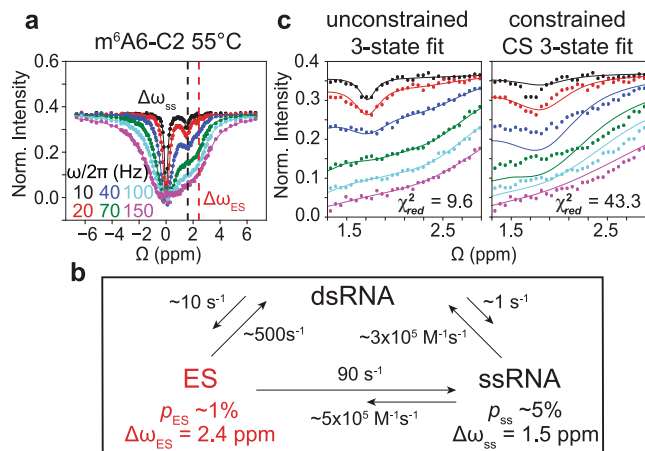


Fig. 3 **A hybridization intermediate for dsGGACU^{m6A6} at $T = 55^\circ C$.** **a** ^{13}C CEST profile for m^6A6 C2 in dsGGACU^{m6A6} at $T = 55^\circ C$ shows a second dip at $\Delta\omega_{ES}$ that is distinct from the ssRNA ES at $\Delta\omega_{ss}$. **b** Exchange parameters (Supplementary Table 3) from a three-state fit to the RD data using a triangular model. **c** Zoom in to the m^6A6 C2 CEST profiles comparing results from an unconstrained three-state fit to the Bloch-McConnell equations assuming the triangular model and a constrained three-state fit assuming a linear CS model. Data for CEST profiles were presented as mean values ± 1 s.d. (smaller than data points) from $n = 3$ independent measurements of peak intensities at zero relaxation delay (see “Methods”).

These results provide a plausible explanation for the unique impact of m^6A on RNA hybridization kinetics at $T = 65^\circ C$. m^6A does not impact the apparent melting rate because the dominant isomer in the duplex is *anti* and it melts at a rate comparable to that of the unmethylated RNA. On the other hand, m^6A slows the apparent annealing rate by ~ 5 -fold due to the ~ 10 -fold lower equilibrium population of the ssRNA^{*anti*} intermediate relative to the unmethylated ssRNA control and because the ssRNA^{*anti*} intermediate anneals at a 2-fold faster rate relative to its unmethylated counterpart.

An additional hybridization intermediate at $T = 55^\circ C$. Although we did not observe any evidence for the IF dsRNA^{*syn*} intermediate, simulations indicate that its RD contribution was probably masked by the larger RD contribution from the ssRNA with a population $\sim 22\%$. We therefore repeated the CEST measurements at a slightly lower temperature $T = 55^\circ C$. This reduced the ssRNA population to $\sim 5\%$, but it remained large enough to permit accurate measurements of hybridization kinetics using NMR RD. Repeating the measurements at a different temperature also allowed us to test the robustness of the CS model. Based on a two-state fit of the adenine C8 RD data, which only reports on a two-state hybridization process (Supplementary Fig. 4a), m^6A reduced the apparent annealing rate by 20-fold while minimally (~ 1.6 -fold) impacting the apparent melting rate under these conditions (Supplementary Fig. 4b).

Interestingly, we observed evidence for an additional ES, which manifested as a second minor dip in the m^6A -C2 CEST profile (Fig. 3a). This ES dip at $\Delta\omega_{C2} \sim 2$ p.p.m. was also observed at lower temperatures in another dsRNA (dsA6RNA^{m6A}) sequence context (Supplementary Fig. 5 and Supplementary Table 1). The fact that this ES was not observed in ssGGACU^{m6A} indicated that it very likely was a dsRNA conformation. The ES was likely not observed at higher temperature $T = 65^\circ C$ (Fig. 2f)²¹ because it

was masked by the higher RD contribution from the more populated ssRNA ES.

The m^6A -C2 RD data (Fig. 3a) could be satisfactorily fit to a three-state model that includes dsRNA, ssRNA, and the additional ES. Among several three-state topologies tested³⁷ (see Supplementary Fig. 4d), the best agreement was obtained with models that place the ES on-pathway between the dsRNA and ssRNA (Fig. 3b). Therefore, these results provide direct evidence for a dsRNA on-pathway hybridization intermediate and the CS pathway alone cannot fully explain the hybridization kinetics at $T = 55^\circ C$. Indeed, simulations using the CS model did not reproduce the m^6A -C2 RD data at $T = 55^\circ C$ ($\chi^2_{red} \sim 600$) (Supplementary Fig. 4c) and neither did a constrained three-state fit to the CS model ($\chi^2_{red} \sim 43.3$) (Fig. 3c) because the model fails to account for the RD contribution from the additional ES.

The dsRNA hybridization intermediate features an $m^6(syn)$ A...U stabilized by a single H-bond. Understanding how m^6A selectively slows annealing of dsGGACU at $T = 55^\circ C$ by 20-fold without affecting the melting rate requires that we characterize the structure of the intermediate, which can be part of a separate hybridization pathway distinct from the CS pathway.

Although never observed previously, one possibility is that the intermediate is a dsRNA conformation in which the methylamino group rotates into the *syn* conformation. Such a conformation is predicted to be highly energetically disfavored in dsRNA, given the loss of at least one Watson-Crick H-bond. However, this loss in energetic stability would be partly compensated for by a gain in the stability of ~ -1.5 kcal/mol from restoring the energetically favored *syn* isomer. Such an intermediate would allow for an IF-type hybridization pathway, in which isomerization of the methylamino group occurs following and not before initial duplex formation (Fig. 1c).

To test this proposed conformation for the ES, we performed an array of NMR RD experiments using a stable hairpin variant of dsGGACU^{m6A} (hpGGACU^{m6A}; Fig. 4a) with a much higher melting temperature (T_m is predicted to be $\sim 80^\circ C$), designed to eliminate any background RD contribution from the ssRNA across a range of temperatures. Interestingly, we observed two-state RD for both m^6A -C10 (Fig. 4b) and m^6A -C2 (Supplementary Fig. 6a) at $T = 55^\circ C$. A global fit of the data yielded an ES population ($\sim 1\%$), k_{ex} ($\sim 500\text{ s}^{-1}$), and $\Delta\omega_{C2} = 2.5$ p.p.m. that were in very good agreement with the values (Supplementary Table 3) measured for the on-pathway ES hybridization intermediate in dsGGACU^{m6A}. The $\Delta\omega_{C10}$ and $\Delta\omega_{C2}$ values were also in very good agreement with values predicted for $m^6(syn)$ A...U based on DFT calculations (Fig. 4g). Additional support that in the ES the methylamino group is *syn* comes from the kinetic rate constants of interconversion (Supplementary Note 1).

To gauge the nature of the Watson-Crick (m^6A)N1...H3-N3(U) H-bond in the ES, we performed additional RD experiments targeting the N3 and H3 atoms of the partner uridine. We observed ^{15}N (Fig. 4c) and 1H (Fig. 4d) RD only for the uridine partner of m^6A (Supplementary Fig. 6a), and the two-state fit of the data yielded exchange parameters similar to those obtained from the carbon C2/C10 data (Supplementary Fig. 6a), indicating that they are reporting on the same ES. The $\Delta\omega_{N3} = -4.8$ p.p.m. and $\Delta\omega_{H3} = -3$ p.p.m. values indicated a substantial weakening of the remaining H-bond in the ES³⁸ (Fig. 4e). Indeed, a structural model for the $m^6(syn)$ A...U ES conformation that predicts the ES chemical shifts well based on DFT (Fig. 4g), and features a slightly (by 0.4 Å) elongated (m^6A) N1...H3-N3(U) H-bond (Supplementary Fig. 6b). Note that while a minor peak was not observed in the 1H CEST profile for U17-

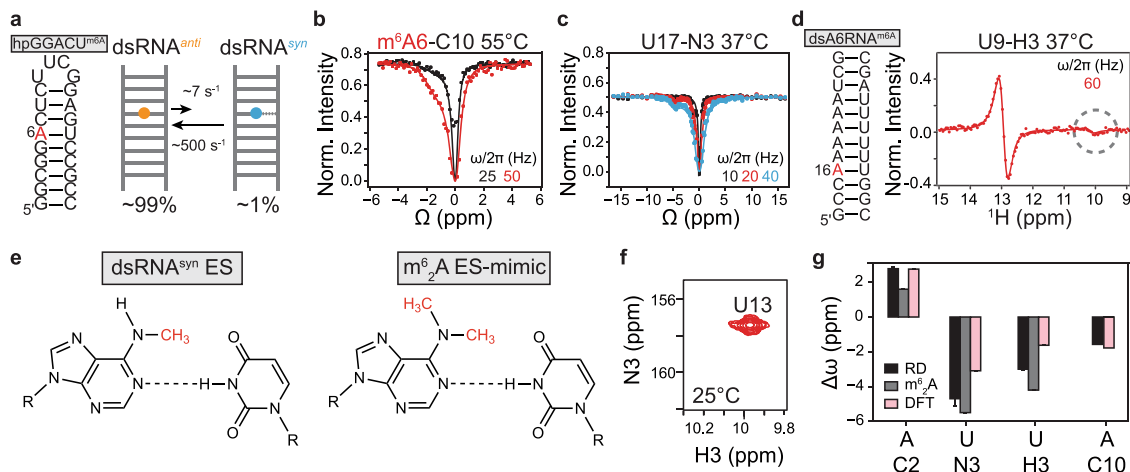


Fig. 4 Characterizing the conformation of the ES intermediate. **a** The hpGGACU^{m⁶A} hairpin construct with the m⁶A site highlighted in red (left) and exchange parameters between dsRNA^{anti} and dsRNA^{syn} measured at $T = 55$ °C (right). **b** ¹³C CEST profile measured for m⁶A6-C10 in hpGGACU^{m⁶A} at $T = 55$ °C. **c** ¹⁵N CEST profile measured for U17-N3 in hpGGACU^{m⁶A} at $T = 37$ °C. **d** The dsA6RNA^{m⁶A} duplex (left) and ¹H CEST profile for U9-H3 at $T = 37$ °C (right). The minor peak is highlighted in the gray circle. **e** Chemical structures of proposed dsRNA^{syn} ES and m⁶A ES-mimic. **f** 2D [¹⁵N, ¹H] HSQC spectra of U13-N3 ¹⁵N-site-labeled dsGGACU^{m⁶A} at $T = 25$ °C. **g** Comparison of the chemical-shift differences ($\Delta\omega_{ES-GS} = \omega_{ES} - \omega_{GS}$) measured using RD in hpGGACU^{m⁶A} (A C2/C10, U-N3) and dsA6^{m⁶A} (U H3) at $T = 37$ °C (RD), when taking the difference between the chemical shifts measured for dsGGACU^{m⁶A} and dsGGACU^{m⁶A} (m⁶₂A) and calculated using DFT as the difference between an m⁶(syn)A...U conformational ensemble and a Watson-Crick m⁶A(anti)-U bp (DFT) (see "Methods" section). Values for m⁶₂A C10 are not shown because it is the site of modification. Solid lines in panels (b-d) denote a fit to the Bloch-McConnell equations to a two-state exchange model (see "Methods"). RF field powers for CEST profiles are color-coded. Data for CEST profiles in panels (b-d) were presented as mean values \pm 1 s.d. (smaller than data points) from $n = 3$ independent measurements of peak intensities at zero relaxation delay (see "Methods"). Data for $\Delta\omega$ (panel g) were presented as mean values \pm 1 s.d. from Monte Carlo simulations (number of iterations = 500) for one CEST measurement as described in "Methods" section. Source data for panel (g) are provided in the Source Data file.

H3 in hpGGACU^{m⁶A}, simulations indicate that this could be due to the 2-fold lower ES population (Supplementary Fig. 6c and Supplementary Table 1).

These results establish that the m⁶A methylamino group can also isomerize even in the context of a duplex m⁶(anti)A-U Watson-Crick bp and show that the preferences for the *syn:anti* isomers is inverted from ~10:1 in the unpaired single-strand to ~1:100 in the paired dsRNA.

Chemical-shift fingerprinting the m⁶(syn)A...U ES using m⁶₂A.

To further verify the unusual m⁶(syn)A...U conformation proposed for the ES, we stabilized this species and rendered it the dominant conformation by replacing the m⁶A amino proton with a second methyl group so as to eliminate the GS Watson-Crick H-bond (Fig. 4e). This N⁶,N⁶-dimethyl adenine (m⁶₂A) modification (Fig. 4e) is also a naturally occurring RNA modification³⁹.

Comparison of NMR spectra of dsGGACU with and without m⁶₂A showed that the modification primarily affected the methylated bp while minimally impacting other neighboring bps (Supplementary Fig. 7a, c). Both the m⁶₂A-C2 and U-N3 chemical shifts of the m⁶₂A-modified dsGGACU (dsGGACU^{m⁶₂A}) were in very good agreement with those measured for the ES in dsGGACU^{m⁶A} using RD (Fig. 4g). In addition, we observed an upfield shifted imino proton resonance (at ~10 p.p.m.), which could unambiguously be assigned via site labeling to the m⁶A partner U13-H3 (Fig. 4f and Supplementary Fig. 7a). This along with nuclear Overhauser effect-based distance connectivity (Supplementary Fig. 7a) indicate that the m⁶(syn)A...U ES likely retains a weaker (m⁶A6)N1...H-N3(U13) Watson-Crick H-bond, although we cannot rule out that the H-bond is mediated by water (see Supplementary Fig. 7e). Similar chemical-shift

agreement including for $\Delta\omega_{H3}$ was obtained for m⁶₂A in dsA6RNA (Supplementary Fig. 7b).

Taken together, these data provide strong support for a singly H-bonded m⁶(syn)A...U bp (Fig. 4e), which is distinct from the bp open state (Supplementary Fig. 8 and Supplementary Note 2). To our knowledge, this alternative m⁶A-specific conformational state has not been documented previously.

m⁶(syn)A...U behaves like a mismatch. Although we initially dismissed hybridization pathways in which the major *syn* isomer hybridizes to form a dsRNA intermediate, our data indicate that this is indeed possible because m⁶A can pair with uridine to form the m⁶(syn)A...U conformation. Several lines of evidence indicate that m⁶(syn)A...U behaves like a mismatch when it comes to hybridization kinetics.

Like many mismatches⁴⁰, m⁶(syn)A...U loses a H-bond and is destabilized relative to the Watson-Crick m⁶(anti)A-U bp by ~3 kcal/mol. In addition, based on the three-state fit of the RD data measured for dsGGACU^{m⁶A} at $T = 55$ °C (Fig. 3b), the m⁶(syn)A...U containing duplex intermediate anneals at a ~20-fold slower rate compared to the unmethylated control, whereas it melts with an ~80-fold faster rate. These changes in hybridization kinetics relative to the unmethylated control are also in line with those previously reported when introducing single mismatches to dsRNA²²⁻²⁴.

We were able to verify the mismatch-like hybridization kinetics of m⁶(syn)A...U containing duplex by using NMR RD to measure the hybridization kinetics of the dsGGACU^{m⁶₂A} ES mimic (Supplementary Fig. 7d). For dsGGACU^{m⁶₂A}, k_{on} was ~16-fold slower, whereas k_{off} was ~100-fold faster relative to the unmethylated RNA. Therefore, depending on the isomer, m⁶A can behave either like a Watson-Crick (*anti*) or mismatch (*syn*) when paired to the same partner uridine.

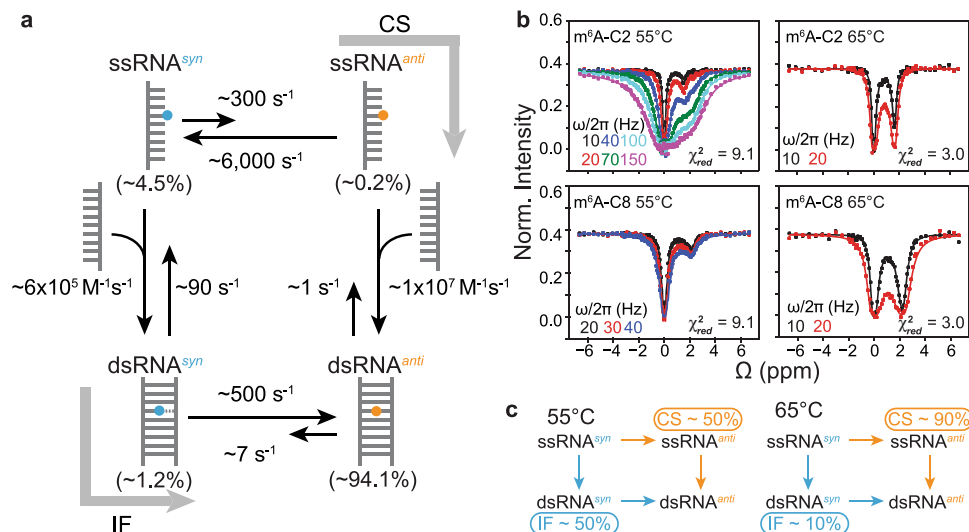


Fig. 5 Testing a four-state CS + IF kinetic model. a Schematic of the CS + IF model with populations and kinetic rate constants measured at $T = 55^\circ\text{C}$ for dsGGACU^{m⁶A}. **b** Constrained four-state (CS + IF model) shared fit (solid lines) of the m⁶A C2 and C8 ¹³C CEST profiles to the Bloch-McConnell equations for dsGGACU^{m⁶A} at $T = 55$ and 65°C . χ_{red}^2 values were obtained from global fitting m⁶A-C2 and m⁶A-C8 CEST data. RF field powers for CEST profiles are color-coded. Data for CEST profiles in panel (b) were presented as mean value \pm 1 s.d. (smaller than data points) from $n = 3$ independent measurements of peak intensities at zero relaxation delay (see “Methods” section). **c** Equilibrium flux through CS and IF pathways at $T = 55$ and 65°C .

Kinetic model for m⁶A hybridization via conformation selection and IF. The RD data measured for dsGGACU^{m⁶A} at $T = 55^\circ\text{C}$ provided direct evidence for hybridization via an IF pathway. However, the standalone IF pathway fails to account for the data measured at both 65°C (Supplementary Fig. 3c) and 55°C (Supplementary Fig. 4e) based on constrained fits. Since the RD data measured at $T = 65^\circ\text{C}$ is consistent with hybridization via CS, with no evidence for flux along IF, we tested a general model that includes both pathways (CS + IF) (Fig. 5a).

We used the four-state CS + IF model along with the exchange parameters ($\Delta\omega$, R_1 , and R_2 values) determined independently (“Methods”) to simulate the RD data measured for dsGGACU^{m⁶A} at $T = 55^\circ\text{C}$. The exchange parameters associated with isomerization in ssRNA were again fixed to the values obtained from temperature-dependent RD measurements on ssGGACU^{m⁶A} (Supplementary Fig. 2c). $k_{\text{off},\text{anti}}$ was again assumed equal to k_{off} and $k_{\text{on},\text{anti}}$ was deduced by using the melting free energy obtained from RD measurements (see “Methods”) (Fig. 2a). $k_{\text{on},\text{syn}}$ and $k_{\text{off},\text{syn}}$ describing the hybridization of ssRNA^{syn} and methyl isomerization in dsRNA were fixed to the values obtained from the three-state fit of the RD data for dsGGACU^{m⁶A} (Fig. 3b).

Indeed, the RD profiles simulated for m⁶A-C2 using the four-state model were in much better agreement ($\chi_{\text{red}}^2 = 10.7$) (Supplementary Fig. 9a) with the experimental data relative to simulations using the CS model ($\chi_{\text{red}}^2 = 563.7$) (Supplementary Fig. 4c) or constrained three-state fits to the CS model ($\chi_{\text{red}}^2 = 43.3$) (Fig. 3c). A constrained fit of the RD data to the four-state model (see “Methods”) improved the agreement further ($\chi_{\text{red}}^2 = 9.6$) (Supplementary Fig. 9a) to a level comparable to the three-state fit (Fig. 3a). The χ_{red}^2 values from globally fitting both m⁶A-C2 and m⁶A-C8 show similar trends (Fig. 5b).

These results provide a plausible explanation for how m⁶A selectively slows dsGGACU^{m⁶A} annealing at $T = 55^\circ\text{C}$ via both the CS and IF pathways. Based on optimized kinetic rate constants obtained from the constrained four-state fit of the RD data, the flux (see “Methods”) was $\sim 50:50$ through the CS and IF

pathways at $T = 55^\circ\text{C}$ (Fig. 5c). Along the CS pathway, m⁶A reduces the apparent rate of annealing due to the ~ 20 -fold lower population of the ssRNA^{anti} intermediate. However, as described for the data measured at $T = 65^\circ\text{C}$, m⁶A does not affect melting because the dominant isomer in the duplex is *anti*, which behaves similarly to unmethylated adenine. Along the IF pathway, m⁶A reduces the apparent rate of annealing by 20-fold because m⁶(*syn*) A \cdots U behaves as a mismatch, reducing hybridization rate to form the dsRNA^{syn} intermediate by 20-fold. Like a mismatch-containing duplex, this intermediate melts at a rate ~ 100 -fold faster relative to the unmethylated duplex. However, the intermediate does not accelerate the apparent melting rate of the methylated duplex along the IF pathway relative to the unmethylated control because its equilibrium population is only $\sim 1\%$.

We also reanalyzed the RD data measured at $T = 65^\circ\text{C}$ and obtained good agreement with the constrained four-state fit ($\chi_{\text{red}}^2 = 3.0$) (Fig. 5b). The level of agreement is similar to that obtained using the constrained three-state fit to the CS model (Fig. 2f), which is expected considering that majority (90%) of the flux is through the CS pathway (Fig. 5c). The smaller flux along the IF pathway at 65 versus 55°C can be attributed to a slower annealing rate along the IF pathway at 65°C due to a 2-fold reduction in the population of the ssRNA^{syn} relative to ssRNA^{anti} and comparatively 2.5-fold slower annealing rate constant of ssRNA^{syn} along the IF pathway relative to ssRNA^{anti} along the CS pathway.

A quantitative model predicts how m⁶A reshapes the hybridization kinetics of DNA and RNA duplexes. To test the generality and robustness of our proposed mechanism, we developed and tested a quantitative CS + IF model that predicts how methylating a central adenine residue impacts the hybridization kinetics for any duplex. The model assumes that the temperature-dependent isomerization kinetics in ssRNA and dsRNA does not vary, consistent with the small deviations (< 2 -fold) seen with sequence, as supported by our data (Supplementary Table 1). The model assumes that $k_{\text{off},\text{anti}} = k_{\text{off}}$ and $k_{\text{on},\text{anti}}$ is deduced based on

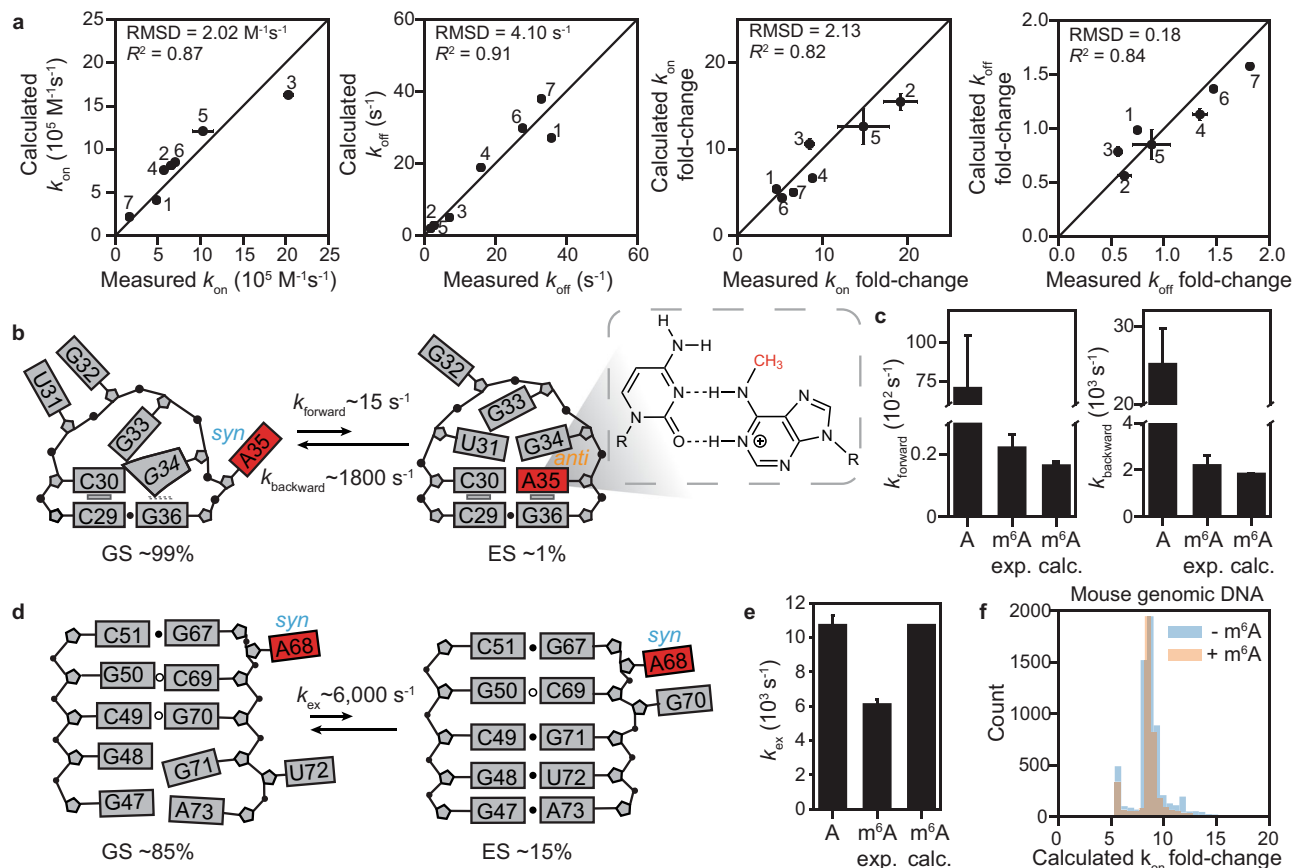


Fig. 6 Testing the predictive power of the CS + IF model. **a** Comparison of experimentally measured and predicted apparent k_{on} , k_{off} , and the fold-change relative to unmethylated duplex (k_{on} fold-change = $k_{on}(\text{unmethylated}) / k_{on,m^6A}^{app}$ and k_{off} fold-change = $k_{off}(\text{unmethylated}) / k_{off,m^6A}^{app}$) for RNA and DNA duplexes. Each point corresponds to a different duplex and/or experimental condition. All buffers contained 40 mM Na^+ , unless stated otherwise: (1) dsGGACU m^6A at $T = 65^\circ\text{C}$, (2) at $T = 55^\circ\text{C}$, (3) with 3 mM Mg^{2+} at $T = 65^\circ\text{C}$; (4) dsHCV m^6A with 3 mM Mg^{2+} at $T = 60^\circ\text{C}$, (5) with 3 mM Mg^{2+} at $T = 55^\circ\text{C}$, (6) with 3 mM Mg^{2+} and 100 mM Na^+ at $T = 60^\circ\text{C}$; (7) dsA6DNA m^6A at $T = 50^\circ\text{C}$. Similar correlations were observed using RD simulation-based prediction method shown in Supplementary Fig. 9b. **b** Secondary structures of GS and ES in the apical loop of HIV-TAR with m^6A35 (highlighted in red), showing the chemical structure of the m^6A^+-C bp. **c** Comparison of $k_{forward}$ and $k_{backward}$ for unmethylated TAR (A), experimentally measured (m^6A exp.) and predicted (m^6A calc.) for methylated TAR. **d** Secondary structures of GS and ES of methylated RREIIB. **e** Comparison of k_{ex} of unmethylated RRE (A), experimentally measured (m^6A exp.), and predicted (m^6A calc.) for methylated RRE. **f** Predicting the m^6A -induced slowdown effect on k_{on,m^6A}^{app} of 12-mers (see “Methods”) for m^6A sites⁹ (orange) and random DNA (blue) in the mouse genome. Data in panels (a, c, e) were presented as mean values ± 1 s.d. from Monte Carlo simulations (number of iterations = 500) for one CEST measurement as described in “Methods.” Source data for panels (a, c, e) are provided in the Source Data file.

the known energetics of annealing the m^6A -containing duplex. The value of $k_{on,syn}$ was assumed to be 20-fold slower than the unmethylated RNA and $k_{off,syn}$ was then deduced by closing the thermodynamic cycle (see “Methods”). Using these rate constants and the CS + IF model, kinetic simulations (see “Methods”) were used to predict k_{on,m^6A}^{app} and k_{off,m^6A}^{app} .

We used the model to predict the k_{on,m^6A}^{app} and k_{off,m^6A}^{app} values recently reported²¹ for two duplexes (dsGGACU m^6A and dsHCV m^6A) under a range of different salt (Mg^{2+} and Na^+) concentrations and temperatures and for an additional dataset involving dsHCV m^6A at $T = 55^\circ\text{C}$ in 3 mM Mg^{2+} (Supplementary Fig. 5). Across these duplexes and conditions, m^6A slowed the apparent annealing by ~ 5 -fold to ~ 20 -fold while minimally impacting the melting rate (< 2 -fold). As shown in Fig. 6a, a good correlation ($R^2 = 0.8$ – 0.9) was observed between the measured and predicted k_{on,m^6A}^{app} and k_{off,m^6A}^{app} , as well as the overall impact on the apparent annealing and melting rates induced by methylation, with all deviations being < 1.5 -fold.

In all the above examples, the equilibrium flux was primarily (~ 50 – 95%) via the CS pathway. The differences in the m^6A -induced slowdown (~ 5 – 20 -fold) of annealing across different duplexes are primarily driven by differences in the annealing rate of ssRNA^{anti} along the CS pathway relative to that of unmethylated RNA, with the slowdown being more substantial the more stable the unmethylated duplex (Supplementary Fig. 9c). It should be noted that the slowdown is predicted to be even more substantial when hybridization is fast and isomerization of methylamino group becomes rate-limiting, as observed for an RNA conformational transition, as described below.

As an additional test, we used the model to predict the impact of m^6A on the apparent hybridization kinetics of an A-rich duplex DNA (dsA6DNA, Supplementary Fig. 5). Based on the unmethylated duplex hybridization kinetics measured previously²¹, the model predicts that m^6A should reduce the apparent k_{on,m^6A}^{app} by ~ 6 -fold while having a little effect (< 2 -fold) on k_{off,m^6A}^{app} . We used NMR RD measurements (Supplementary

Fig. 5) on methylated dsA6DNA to test these predictions and the results show that m^6A reduces k_{on,m^6A}^{app} by ~ 8 -fold while having a little effect (<2 -fold) on k_{off,m^6A}^{app} , in good agreement with the predictions (Fig. 6a).

Finally, we extended our model to also predict NMR CEST data by imposing additional constraints on NMR exchange parameters ($\Delta\omega$, R_1 , and R_2) needed to simulate the RD data (see “Methods”). In addition to providing a rationale for the kinetic basis of the m^6A -induced hybridization slow down, such a model would also validate the existence of the IF and CS intermediates in diverse sequence contexts under a variety of experimental conditions. Thus, we subjected all of the above RD data to a constrained four-state fit to the CS + IF model. A reasonable fit ($\chi_{red}^2 \sim 3.5$ – 14) could be obtained in all cases (Supplementary Fig. 9d). This suggests that m^6A -induced hybridization slowdown in DNA is likely mediated by similar IF and CS intermediates as RNA.

Testing kinetic model on RNA conformational transitions.

Beyond duplex hybridization, our kinetic model predicts that m^6A should also slow intramolecular conformational dynamics in which m^6A transitions between an unpaired conformation, in which the methylamino group is predominantly *syn*, and a paired conformation, in which the methylamino group is predominantly *anti*. In addition, the model predicts that the slowdown can be much more substantial for conformational transitions that are much faster than the hybridization kinetics measured under our experimental conditions.

To test these predictions, we methylated A35 in the apical loop of transactivation response element (TAR) (Fig. 6b) from human immunodeficiency virus type-1 (HIV-1)⁴¹ and examined whether m^6A reduces the rate constant of a previously described intramolecular conformational transition in which unpaired A35 in the GS forms a wobble A35⁺-C30 mismatch in the ES⁴². As in the Watson–Crick A–U bp, the methylamino group needs to be *anti* to form one of the H-bonds in the m^6A^+ -C wobble (Fig. 6b). TAR therefore also allowed us to test the generality of the model to non-Watson–Crick bps.

We prepared a TAR NMR sample containing m^6A A35 and ¹³C8-labeled G34 as an RD probe⁴². Based on the chemical-shift perturbations, m^6A destabilized the TAR ES relative to the GS by ~ 2 kcal/mol, in a manner analog to duplex destabilization¹² (Supplementary Fig. 10a and “Methods”). The CS + IF kinetic model predicts that m^6A will reduce k_{ex} , $k_{forward}$ and $k_{backward}$ for the TAR conformational transition by ~ 17 -, ~ 400 -, and ~ 14 -fold, respectively. The much greater m^6A induced reduction in the forward rate constant relative to hybridization arises because the TAR conformational transition is intrinsically faster, and this pushes the isomerization step in the dominant CS pathway away from equilibrium, leading to a slowdown much greater than that due to the equilibrium population ($\sim 10\%$) of the ssRNA^{anti} CS intermediate when hybridization is limiting. Here, the IF pathway is highly disfavored (flux $< 1\%$) because the ES with m^6A in the *syn* conformation is predicted to be highly energetically disfavored.

Based on NMR RD measurements (Supplementary Fig. 10b), m^6A reduced k_{ex} , $k_{forward}$, and $k_{backward}$ by ~ 15 -, ~ 300 -, and ~ 12 -fold in very good agreement with predictions from our model (Fig. 6c). The TAR experimental RD data could be satisfactorily fit to a constrained three-state fit to the CS model with $\chi_{red}^2 = 0.2$ (Supplementary Fig. 10c) comparable to that obtained from an unconstrained two-state fit. These results indicate that m^6A can also slow down RNA conformational transitions and potentially to a much greater degree than observed in our duplex hybridization experiments.

As a negative control, m^6A minimally (<2 -fold) affects the exchange rate of conformational transition in the HIV-1 Rev response element stem IIB (RREIIB; Fig. 6d)⁴³ in which the m^6A remains unpaired in the two conformations (Fig. 6e, Supplementary Fig. 10d, and Supplementary Note 3).

Discussion

Our results help explain how m^6A selectively and robustly slows annealing while minimally impacting the rate of duplex melting under our experimental conditions. The minor ssRNA^{anti} isomer hybridizes with kinetic rate constants similar to unmethylated adenine. m^6A slows the apparent annealing rate along the CS pathway relative to the unmethylated control due to the low equilibrium population of the ssRNA^{anti} isomer. Once in a duplex, *anti* is the dominant isomer and m^6A does not substantially impact the apparent rate of duplex melting along the CS pathway. The major ssRNA^{syn} isomer can also hybridize via an IF pathway to form a singly H-bonded bp and with kinetic rate constants similar to that of a mismatch-containing duplex. This intermediate forms slowly, explaining why m^6A also slows the apparent annealing rate along the IF pathway. However, because its equilibrium population is only $\sim 1\%$, the intermediate does not accelerate the apparent melting rate along the IF pathway. While we have focused on relatively short duplexes with m^6A located in the middle, the impact of the modification on the hybridization kinetics will likely vary and be diminished when placed near the terminal ends, as observed for mismatches²².

By treating the two m^6A isomers as two modular elements that have Watson–Crick or mismatch-like kinetic properties independent of sequence context⁴⁴, we were able to build a model that can predict the impact of m^6A on the overall hybridization kinetics and RNA conformational dynamics from component reactions. The power of such a quantitative and predictive kinetic model is that it obviates the need to carry out time-consuming kinetics experiments to measure the universe of kinetics data that is of biological interest. For example, when combined with an existing computational model that can predict the hybridization kinetics of unmethylated DNA duplexes from sequence⁴⁵, our model could be used to predict how a central m^6A impacts the hybridization kinetics of any arbitrary DNA duplex. This allowed us to predict the impact of m^6A on hybridization kinetics for all ~ 6000 m^6A sites reported in the mouse genome⁹ (Fig. 6f). Our model may also aid the design and implementation of studies that harness the kinetic effects of m^6A as a chemical tool that can bring conformational transitions within detection or aid kinetic studies of RNA and DNA biochemical mechanisms.

Our model also makes a number of interesting biological predictions. The model predicts that m^6A should slow any process in which the unpaired m^6A in the predominantly *syn* isomer has to transition into a conformation in which m^6A is predominantly *anti*. This should include all templated processes that create canonical A–U Watson–Crick bps and many mismatches (A⁺ (*anti*)–C (*anti*), A (*anti*)–G (*anti*), and A⁺ (*anti*)–G (*syn*)), in which the methylamino group adopts the *anti* conformation. m^6A is found in a variety of RNAs involved in processes that require base pairing, including R-loop formation⁴⁶, microRNA RNA target recognition⁴⁷, snoRNA–pre-rRNA base pairing⁴⁸, snRNA–pre-mRNA base pairing⁴⁹, and the assembly of the spliceosome⁵⁰ and ribosome⁵¹. The model also predicts that the m^6A -induced slowdown could exceed 1000-fold for fast conformational transitions such as the folding of short hairpins and this could have important consequences on RNA folding, conformational switches, RNA protein recognition, and processes that occur co-transcriptionally. Further studies are needed to

examine whether m⁶A does indeed slow these processes and whether this has any biological consequences.

Our NMR measurements had to be performed under high-temperature conditions so that hybridization falls within the detection limits of RD. However, we were able to observe isomerization of the methylamino group in both ssRNA and dsRNA at $T = 37^\circ\text{C}$ (Supplementary Figs. 2b and 6a). Based on the temperature dependence of the hybridization steps in the CS and IF pathways, our model predicts (see “Methods”) that m⁶A will slow down annealing by ~5-fold while minimally impacting the melting rate consistent with our measurements at higher temperatures. A comparable level of the slowdown in annealing is also obtained when predicting the m⁶A-induced slowdown at $T = 37^\circ\text{C}$ using rate constants for hybridization of unmethylated RNA reported previously²² at $T = 37^\circ\text{C}$ and assuming that m⁶A destabilizes dsRNA by 1 kcal/mol⁵² (see “Methods”).

The mismatch-like m⁶(syn)A...U bp is interesting not only because of its role in hybridization kinetics but also because it could potentially prime the methylamino group for recognition by reader proteins, which recognize the methylamino group in a *syn* conformation⁵³. Upon surveying ~50,000 unmethylated A–U bps in Protein Data Bank (PDB), we found 428 bps that share the conformational signatures of the singly H-bonded m⁶A...U bp (see “Methods”). More than 60% of these bps are found in noncanonical regions, such as junctions, terminal ends, tertiary structural elements, and protein-bound RNA (Supplementary Fig. 7f). It will be interesting to examine whether the mismatch-like m⁶(syn)A...U forms as the dominant conformation in certain structural contexts where it may facilitate recognition by reader proteins both by locally destabilizing the bp, so that m⁶A is more accessible and by adopting a preformed *syn* conformation.

Methods

Sample preparation

AMP and m⁶AMP. Unlabeled adenosine and N⁶-methyladenosine 5'-monophosphate monohydrate (AMP and m⁶AMP) were purchased from Sigma-Aldrich (A2252 and M2780). Powders were directly dissolved in NMR buffer (25 mM sodium chloride, 15 mM sodium phosphate, 0.1 mM EDTA, and 10% D₂O at pH 6.8 with or without 3 mM Mg²⁺). The final concentrations of AMP and m⁶AMP were 50 mM.

Oligonucleotides. Unmethylated, methylated (N⁶-methylated adenosine, N⁶,N⁶-dimethyl adenosine), and ¹³C- or ¹⁵N-site-labeled (¹⁵N₃-labeled U, ¹³C₈, ¹³C₂-labeled A/m⁶A, and ¹³C₁₀-labeled m⁶A) RNA oligonucleotides were synthesized using a MerMade 6 Oligo Synthesizer employing 2'-tBDSilyl-protected phosphoramidites and 1 μmol standard synthesis columns (1000 Å) (BioAutomation). Unlabeled m⁶A, m²A, rU, and *n*-acetyl-protected rC, rA, and rG phosphoramidites were purchased from Chemgenes. ¹⁵N₃-labeled U and ¹³C₈, ¹³C₂-labeled rA/m⁶A phosphoramidites were synthesized in-house according to published procedures^{21,36}. ¹³C₁₀-labeled m⁶A phosphoramidite was synthesized as described in Supplementary Note 4. RNA oligonucleotides were synthesized with the option to retain the final 5'-protecting group, 4,4'-dimethoxytrityl (DMT). Synthesized oligonucleotides were cleaved from columns using 1 ml AMA (1:1 ratio of 30% ammonium hydroxide and 30% methylamine), followed by 2-h incubation at room temperature. The solution was then air-dried and dissolved in 115 μl dimethyl sulfoxide, 60 μl triethylamine (TEA), and 75 μl TEA.3HF, followed by 2.5-h incubation at $T = 65^\circ\text{C}$ for 2'-O deprotection. The solutions were then quenched using Glen-Pak RNA quenching buffer and loaded onto Glen-Pak RNA cartridges (Glen Research Corporation) for purification and subsequently ethanol precipitated. Following ethanol precipitation, RNA oligonucleotides were dissolved in water (200–500 μM for duplex samples, 50 μM for hairpin samples) and annealed by heating an equimolar amount of complementary single strands or hairpins at $T = 95^\circ\text{C}$ for 10 min, followed by cooling at room temperature for 2 h for duplex samples or 30 min on ice for hairpin samples. Extinction coefficients for concentration calculation were obtained from the atdbio online calculator (<https://www.atdbio.com/tools/oligo-calculator>). The extinction coefficients for modified single strands were assumed to be equal to that of their unmodified counterparts. All samples were buffer exchanged using centrifugal concentrators (Amicon Ultra-15 3-kDa cut-off EMD Millipore) into NMR buffer (25 mM sodium chloride,

15 mM sodium phosphate, 0.1 mM EDTA, and 10% D₂O at pH 6.8 with or without 3 mM Mg²⁺).

The ¹³C₈, ¹³C₂-labeled m⁶dA ssA6DNA oligonucleotide was synthesized in-house using a MerMade 6 oligo synthesizer. The ¹³C₈, ¹³C₂-labeled m⁶dA phosphoramidite was synthesized as described in Supplementary Note 5. Standard DNA phosphoramidites (*n*-ibu-dG, bz-dA, ac-dC, and dT) were purchased from Chemgenes. DNA oligonucleotides were synthesized with the option to retain the final 5'-DMT group. Synthesized oligonucleotides were cleaved from columns using 1 ml AMA, followed by 2-h incubation at room temperature. The DNA sample was then purified using Glen-Pak DNA cartridges and ethanol precipitated. The complementary ssDNA of the m⁶A containing ssDNA is uniformly ¹³C/¹⁵N labeled and was synthesized and purified by in vitro primer (see Supplementary Table 8) extension⁵⁴ using ¹³C/¹⁵N isotopically labeled dNTPs (Silantes), and purified using 20% 29:1 polyacrylamide denaturing gel with 8 M urea, 20 mM Tris borate, and 1 mM EDTA, and electroelution (Whatmann, GE Healthcare) in 40 mM Tris acetate and 1 mM EDTA. DNA duplexes were prepared and buffer exchanged in a manner analogous to that described above for RNA duplexes.

Definition of rate constants.

1. k_1 and k_{-1} are the forward and backward rate constants for methylamino isomerization in ssRNA, respectively.
2. k_2 and k_{-2} are the forward and backward rate constants for methylamino isomerization in dsRNA, respectively.
3. k_{on} and k_{off} are the annealing and melting rate constants, respectively, for unmethylated RNA.
4. $k_{\text{on,anti}}$ and $k_{\text{off,anti}}$ are the annealing and melting rate constants, respectively, when m⁶A adopts *anti* conformation in both ssRNA and dsRNA.
5. $k_{\text{on,syn}}$ and $k_{\text{off,syn}}$ are the annealing and melting rate constants, respectively, when m⁶A adopts *syn* conformation in both ssRNA and dsRNA.
6. $k_{\text{on,m6A}}^{\text{app}}$ and $k_{\text{off,m6A}}^{\text{app}}$ are the apparent annealing and melting rate constants, respectively, for m⁶A-methylated RNA.
7. k_{forward} and k_{backward} are the forward and backward rate constants, respectively, for conformational transitions measured using RD.

NMR experiments

Resonance assignments. All NMR experiments (except for the imino proton exchange experiment) were performed on a Bruker Avance III 600 MHz spectrometer equipped with a 5 mm triple-resonance HCPN cryogenic probe. Resonance assignments for hpGGACU^{m⁶A} have been reported previously³⁶. Resonance assignments for m⁶A-modified dsGGACU and dsA6 were obtained using 2D [¹H, ¹H] nuclear magnetic resonance spectroscopy experiments with 150 ms mixing time along with 2D [¹³C, ¹H] and [¹⁵N, ¹H] Heteronuclear single quantum coherence spectroscopy (HSQC) experiments. The assignments for ssGGACU^{m⁶A}, ssA6RNA^{m⁶A}, dsGGACU A/m⁶A, dsA6DNA^{m⁶A}, and dsHCV A/m⁶A could be readily obtained since the samples were site-specifically labeled. The assignments for AMP and m⁶AMP were obtained from a prior study²⁵ (Supplementary Fig. 1). Data were collected using TopSpin 3.2 (Bruker), processed using NMRpipe software package⁵⁵, and analyzed using SPARKY (T.D. Goddard and D.G. Kneller, SPARKY 3, University of California, San Francisco).

¹³C and ¹⁵N R_{1ρ} relaxation dispersion. ¹³C and ¹⁵N R_{1ρ} experiments were performed using 1D R_{1ρ} schemes as described previously^{56–58}. The spin-lock powers ($\omega/2\pi$ Hz) and offsets ($\Omega_{\text{eff}}/2\pi$ Hz, where $\Omega_{\text{eff}} = \omega_{\text{obs}} - \omega_{\text{rf}}$, where ω_{obs} is the Larmor frequency of the spin and ω_{rf} is the carrier frequency of the applied spin-lock) are listed in Supplementary Table 5. The spin-lock was applied for a maximal duration (<120 ms for ¹⁵N and <60 ms for ¹³C) to achieve ~70% loss of peak intensity at the end of the relaxation delay.

Analysis of R_{1ρ} data. 1D peak intensities were measured using NMRpipe⁵⁵. R_{1ρ} values for a given spin-lock power and offset combination were calculated by fitting the intensities as a function of delay time to a monoexponential decay³⁴. A Monte Carlo approach was used to calculate R_{1ρ} uncertainties⁵⁹. Alignment of initial magnetization during the B–M fitting was performed based on the $k_{\text{ex}}/|\Delta\omega_{\text{major}}|$ ratio ($k_{\text{ex}}/|\Delta\omega_{\text{major}}| \geq 1$ and $k_{\text{ex}}/|\Delta\omega_{\text{major}}| > 1$ corresponding to GS alignment and AVG alignments, respectively)¹⁸. Chemical exchange parameters were obtained by fitting experimental R_{1ρ} values to numerical solutions of the B–M equations³² that describe N-site chemical exchange³⁴. Errors in exchange parameters were determined using a Monte Carlo approach³⁴. When available, R_{1ρ} data measured for the same exchange process under the same condition were globally fitted, sharing ES population and exchange rate constants. Reduced χ^2 ($\chi_{\text{red}}^2 = \sum_{i=1}^N \left(\frac{R_{1\rho(i)}^{\text{Calc}} - R_{1\rho(i)}^{\text{Exp}}}{\sigma_{\text{exp}(i)}} \right)^2$), $R_{1\rho(i)}^{\text{Calc}}$, and $R_{1\rho(i)}^{\text{Exp}}$ are experimentally measured and calculated R_{1ρ} data using the B–M equations, $\sigma_{\text{exp}(i)}$ is the experimental uncertainty in R_{1ρ} determined using a Monte Carlo approach) was calculated to assess the goodness of fitting¹⁸. In

general, similar exchange parameters were obtained from individual fitting and global fitting. All exchange parameters are summarized in Supplementary Table 1.

Estimate p_{ES} of methylated TAR from chemical shifts. The RD signal of methylated TAR is weak probably due to small p_{ES} and fast k_{ex} (Supplementary Fig. 10b). We used chemical-shift perturbation-based method⁶⁰ as an alternative approach to estimate the population of ES⁴² (p_{ES,m^6A}) of methylated TAR. Specifically, in methylated TAR, $\omega_{obs} = \omega_{GS} \times (1 - p_{ES,m^6A}) + \omega_{ES} \times p_{ES,m^6A}$. ω_{GS} and ω_{ES} are chemical shifts of GS and ES of unmethylated TAR and were determined previously⁶⁰. Based on 2D [¹³C, ¹H] HSQC spectra, G34-C8 peak shifts toward GS (Supplementary Fig. 10a), and the calculated p_{ES,m^6A} is ~1%.

¹³C and ¹⁵N CEST. ¹³C and ¹⁵N CEST experiments were performed using 1D schemes without equilibration of GS and ES magnetization prior to the relaxation delay²¹. The RF field strengths ($\omega/2\pi$ Hz) and offset combinations ($\Omega/2\pi$ Hz, where $\Omega = \omega_{rf} - \omega_{obs}$) used in CEST measurements are listed in Supplementary Table 6. The relaxation delay for all CEST experiments was 200 ms.

2D CEST for ¹³C methyl probes. The pulse sequence for the ¹³C methyl CEST was derived by modifying the 2D CEST experiment for ¹³C from Zhang and co-workers²⁹ in accordance with considerations described in Bouvignies and Kay³¹ outlining a 2D CEST experiment for ¹³C methyl groups. The following changes were made to the CEST experiment from Zhang and co-workers²⁹:

- Given that the samples for methyl CEST in this study were site specifically ¹³C labeled at the methyl group, we removed shaped pulse c that was used to refocus carbon-carbon scalar couplings.
- The delay τ between ¹³C pulses of phases ϕ_2 and ϕ_3 and ϕ_3 and ϕ_5 was set to be as close as possible to the optimal value of $\tau = \frac{\arccos(\sqrt{2/3})}{2\pi J_{HC}}$, where J_{HC} is the scalar coupling between the methyl carbon and protons, and for optimal transfer of in-phase methyl carbon magnetization to antiphase, as described by Bouvignies and Kay, while ensuring that the delays between the pulses in the sequence were positive. J_{HC} was measured using an FI-coupled 2D [¹³C, ¹H] HSQC experiment.
- The τ delay flanking shaped pulse b was set to be equal to $\frac{\arccos(\sqrt{1/3})}{2\pi J_{HC}}$. The duration of shaped pulse b was shortened as needed so as to ensure that the delays between the pulses in the sequence were positive.
- A gradient pulse was inserted between the ¹³C and ¹H $\pi/2$ pulses after T1 evolution, as described by Bouvignies and Kay³¹, to purge transverse magnetization.

Analysis of the CEST data. 1D or 2D peak intensities were calculated using NMRpipe⁵⁵. The intensity error for all offsets for a given spin-lock power was set to be equal to the standard deviation of three measurements of peak intensity with zero relaxation delay under the same spin-lock power. The intensities were normalized to the average intensity of the three zero delay measurements. Exchange parameters were then obtained by fitting experimental intensity values to numerical solutions of the B-M equations and RF field inhomogeneity was taken into account during CEST fitting⁶¹. No equilibration of GS magnetization was assumed when integrating the B-M equations for non-methyl probes⁶¹, while equilibration was assumed for the methyl CEST given that the sequence employs nonselective hard pulses. Fits of CEST data were carried out assuming unequal R_2 or assuming equal R_2 for duplex melting²¹ and other ES measurements, respectively. Alignment of the initial magnetization during CEST fitting was chosen based on the $k_{ex}/|\Delta\omega_{major}|$ ratio as described in the previous section⁶¹. Errors in exchange parameters were determined using a Monte Carlo approach with 500 iterations⁶². Global fitting of CEST data was carried out for the same exchange process under identical conditions. χ^2_{red} was calculated to assess the goodness of fitting as described in the previous section¹⁸. Note that the different χ^2_{red} values for different fits are most likely due to differences in the quality of the NMR data and poor estimation of the real experimental uncertainty (Supplementary Table 1). Model selection (three state with triangular, linear, or starlike topology; Supplementary Fig. 4d) was carried out by calculating Watanabe-Akaike information criterion and Watanabe-Bayesian information criterion weights for each model and selecting the model with the highest relative probability³⁴.

¹H CEST experiment. A transverse relaxation optimized spectroscopy-based spin-state selective ¹H CEST experiment⁶³ was carried as described previously⁶⁴. The power of the B_1 field was set to be 60 or 120 Hz and the offset of the B_1 field ranged from 8.5 p.p.m. to 15.5 p.p.m. with a step of 30 Hz. The relaxation delay was 400 ms. The ¹H CEST data were collected in a pseudo-3D mode and were analyzed using NMRPipe⁵⁵. The intensities in the N^α and N^β CEST profiles were normalized to a reference intensity with B_1 frequency = -20 p.p.m. The N^β CEST profile was then subtracted from the N^α CEST profile to result in a difference CEST profile, from which the $\Delta\omega$ of the ES was fitted with predetermined fitting parameters such as p_{ES} , k_{ex} and ¹⁵N R_1 from the ¹³C/¹⁵N $R_{1\rho}$ experiments. Errors in the CEST intensity profiles were estimated based on the scatter in regions of 1D profiles that

did not contain any intensity dips. The Python package ChemEx (<https://github.com/gbouvignies/chemex>) is used to carry out the fitting.

Imino proton exchange experiment. Experiments were carried out on a 700 MHz Bruker NMR spectrometer equipped with hydrogen cyanide room-temperature probe to measure the proton exchange between imino proton and water⁶⁵, following the same pulse programs and protocols as described in a prior study⁶⁶. Briefly, the water proton longitudinal relaxation rate constant R_1 was first measured using a standard saturation-recovery method⁶⁶. A pre-saturation pulse was used for solvent suppression. The relaxation delay time for measuring water proton R_1 was set to be 0.0, 0.4, 0.8, 1.2, 1.6, 2.0, 2.4, 2.8, 3.2, 3.6, 4.0, 4.4, 4.8, 5.2, 6.0, 7.0, 8.0, 9.0, 10.0, 12.0 and 15.0 s. The apparent solvent exchange rate constant of the imino protons was then measured using an inversion-recovery scheme by initially selectively inverting the bulk water magnetization, followed by detecting transfer of the water magnetization to the imino proton during the solvent exchange. A sinc-shaped π -pulse was optimized and used to invert the water magnetization. A binominal water-suppression scheme was used to suppress water. The delay times used to measure water and imino proton exchange rate constants are listed in Supplementary Table 7.

The apparent exchange rate (k_{ex}) of imino and water proton was obtained by fitting the imino magnetization as a function of exchange time upon solvent exchange according to Eq. (1),

$$W(t) = W^0 - E \times W^0 \times \frac{k_{ex}}{R_{1w} - R_{1i}} \times (e^{-R_{1i} \times t} - e^{-R_{1w} \times t}) \quad (1)$$

where $W(t)$ is the imino peak volume as a function of exchange time t , W^0 is the initial peak volume (at $t = 0$ s), E is the efficiency of the inversion pulse, k_{ex} is the apparent solvent exchange rate constant between imino and water proton, R_{1w} is water proton R_1 , R_{1i} is the summation of imino proton R_1 , and exchange rate constant k_{ex} . In the equation, R_{1w} and E values are fixed parameters that are predetermined, while k_{ex} and R_{1i} are fitted parameters. The error of the fitted parameters is the standard fitting error, which is the square root of the diagonal elements of the covariance matrix. The efficiency of the selective shaped pulse used for water inversion (E) was calculated by Eq. (2):

$$E = 1 - \frac{W_{inv}}{W_{eq}} \quad (2)$$

where W_{inv} and W_{eq} represent the peak volumes of the water proton with and without the shaped pulse for inversion, respectively (at zero delay time and without binominal water suppression).

Determining the methylamino isomerization rate constants from temperature-dependent RD measurements for methylated ssRNA and dsRNA. The observed temperature dependence of k_1 , k_{-1} in m⁶AMP and ssRNA (Supplementary Fig. 2c) and k_2 , k_{-2} in dsRNA (Supplementary Fig. 6d) determined using RD were fit to a modified van't Hoff equation that accounts for statistical compensation effects and assumes a smooth energy surface⁵⁷:

$$\ln\left(\frac{k_i(T)}{T}\right) = \ln\left(\frac{k_B \kappa}{h}\right) - \frac{\Delta G_i^\ddagger(T)}{RT_{hm}} - \frac{\Delta H_i^\ddagger(T)}{R} \left(\frac{1}{T} - \frac{1}{T_{hm}}\right) \quad (3)$$

where k_i ($i = 1, -1$ or $2, -2$) is the rate constant, $\Delta G_i^\ddagger(T)$ and $\Delta H_i^\ddagger(T)$ are the free energy and enthalpy of activation ($i = 1, 2$) or deactivation ($i = -1, -2$), respectively, R is the universal gas constant (kcal/mol/K), T is temperature (K), and T_{hm} is the harmonic mean of the experimental temperatures (T_i in K) computed as

$$T_{hm} = n / \sum_{i=1}^n (1/T_i), \quad k_B \text{ is the Boltzmann's constant, } \kappa \text{ is the transmission coefficient (assumed to be 1). The goodness-of-fit indicator } R^2 \text{ between the measured and fitted rate constants was calculated as follows:}$$

$R^2 = 1 - \frac{SS_{res}}{SS_{total}}$, $SS_{res} = \sum (k_{i,fit} - k_{i,exp})^2$, $SS_{total} = \sum (k_{i,exp} - \bar{k}_{i,exp})^2$. $k_{i,fit}$ and $k_{i,exp}$ ($i = 1, -1$ or $2, -2$) are fitted and experimentally measured rate constants. $\bar{k}_{i,exp}$ is the mean of all $k_{i,exp}$. Errors of fitting for $\Delta G_i^\ddagger(T)$ and $\Delta H_i^\ddagger(T)$ were calculated as the square root of the diagonal elements of the covariance matrix. Given these fitted $\Delta G_i^\ddagger(T)$ and $\Delta H_i^\ddagger(T)$ values, k_i at $T = 55$ and 65 °C used for kinetic modeling was computed using Eq. (3).

Measuring the kinetics of duplex hybridization from CEST data. k_{off} (s^{-1}) and k_{on} ($M^{-1} s^{-1}$) for duplex hybridization were determined based on the forward rate ($k_{forward}$) and backward ($k_{backward}$) rate constants obtained from a two-state fit of the dsHCV/dsHCVm⁶A A11-C8 and dsA6DNA m⁶A16-C2 RD data (two-state fit of other constructs were reported previously²¹) and a three-state fit of m⁶A-C2 dsGGACUm⁶A at $T = 55$ °C:

$$k_{forward} = k_{off} \quad (4)$$

$$k_{backward} = k_{on} \times [ss2] \quad (5)$$

where $[ss2]$ is the free concentration of the complementary single strand.

$$k_{backward} = k_{ex}(1 - p_{ss}) \quad (6)$$

where p_{ss} is the single-strand population. The annealing rate constant k_{on} is given by:

$$k_{on} = \frac{k_{ex}(1 - p_{ss})}{[ss2]} \quad (7)$$

The uncertainty in [ss2], and p_{ss} and k_{ex} from CEST measurements were propagated to determine the uncertainty in k_{on} . From two-state CEST fit, [ss2] = $C_t \times p_{ss}$, where C_t is the total concentration of the duplex, which was obtained using the extinction coefficient as described in the ‘‘Sample preparation’’ section. The uncertainty of C_t was assumed to be 20%²¹. [ss2] from a three-state fit were calculated as described in the energetic decomposition section below.

Validation of NMR RD measurements on m⁶A RNA hybridization. We have previously²¹ shown that hybridization kinetics measured from NMR RD on unmodified DNA and RNA duplexes are consistent with those measured using other techniques employing fluorescence spectroscopy. As an additional test, we performed temperature-dependent RD measurements for dsGGACU^{m⁶A} (Supplementary Fig. 11a). The annealing rate constant k_{on} did not have a strong temperature dependence, consistent with prior studies reporting non-Arrhenius behavior for k_{on} in unmodified duplexes^{67,68}. On the other hand, the melting rate constant k_{off} showed a strong temperature dependence, which was also consistent with prior studies^{67,68}. The extrapolated annealing thermodynamic parameters including ΔG_{anneal}° , ΔH_{anneal}° , and ΔS_{anneal}° measured from NMR experiments are in good agreement with those measured from ultraviolet (UV) melting experiments³⁶ (Supplementary Fig. 11b, c). We also observed a good agreement between the annealing free energy (ΔG_{anneal}°) measured using CEST and UV melting experiments for nine additional DNA/RNA duplexes at temperatures ranging from 45 to 65 °C²¹ (Supplementary Fig. 11d).

UV melting experiments. UV melting experiments were conducted on a PerkinElmer Lambda 25 UV/VIS spectrometer with an RTP 6 Peltier Temperature Programmer and a PCB 1500 Water Peltier System. At least three measurements were carried out for each sample (3 μ M in NMR buffer without D₂O) with a volume of 400 μ l in a Teflon-stoppered 1 cm path length quartz cell. The absorbance at 260 nm (A_{260}) was monitored at temperatures ranging from 15 to 95 °C, and at a ramp rate of 1.0 °C/min. The melting temperature (T_m) and standard enthalpy change (ΔH°) of hybridization reaction for duplexes were obtained by fitting the absorbance of the optical melting experiment to Eqs. (8) and (9)⁶⁹,

$$A_{260} = ((m_{ss} \times T) + b_{ss}) \times p_{ss} + ((m_{ds} \times T) + b_{ds}) \times (1 - p_{ss}) \quad (8)$$

$$p_{ss} = 1 - \frac{1 + 4e^{\left(\frac{1}{T_m} - \frac{1}{T}\right) \frac{\Delta H^\circ}{R}} - \sqrt{1 + 8e^{\left(\frac{1}{T_m} - \frac{1}{T}\right) \frac{\Delta H^\circ}{R}}}}{4e^{\left(\frac{1}{T_m} - \frac{1}{T}\right) \frac{\Delta H^\circ}{R}}} \quad (9)$$

where m_{ss} , b_{ss} , m_{ds} , and b_{ds} are coefficients describing the temperature dependence of the molar extinction coefficient of single strands and double strands, respectively, T is the temperature (K), R is the gas constant (kcal/mol/K), and p_{ss} is the population of the single strand. Standard entropy change (ΔS°) and ΔG° of double-strand hybridization were therefore computed from Eqs. (10) and (11):

$$\Delta S^\circ = \frac{\Delta H^\circ}{T_m} - R \ln\left(\frac{C_t}{2}\right) \quad (10)$$

$$\Delta G^\circ = \Delta H^\circ - T \Delta S^\circ \quad (11)$$

where C_t is the total concentration of duplex. The uncertainty in T_m and ΔH° were obtained based on standard deviation in triplicate measurements that were propagated to the uncertainty of ΔS° and ΔG° .

MD simulations. To generate an ensemble of RNA duplexes with different m⁶A geometries, we performed MD simulations on dsGGACU with the m⁶A–U bp in either *syn* or *anti* conformations, or an m⁶2A...U bp. All MD simulations were performed using the ff99 AMBER force field with bsc0 and χ_{OL3} corrections for RNA, using periodic boundary conditions as implemented in the AMBER MD package. Starting structures for MD of unmethylated dsGGACU were generated by building an idealized A-RNA duplex using the *fiber* module of the 3DNA suite of programs⁷⁰. The starting structures for dsGGACU^{m⁶A} with an m⁶A–U bp in either the *anti* or *syn* conformation were generated by replacing the *anti* and *syn* adenine amino hydrogen atoms in the idealized unmethylated dsGGACU structure with a methyl group. The starting structure for the dsGGACU duplex with the m⁶2A–U bp was generated by replacing both of the amino hydrogen atoms of the adenine in the idealized unmethylated dsGGACU structure with methyl groups. All starting structures were solvated with an octahedral box of SPC/E water molecules with box size chosen such that the boundary was at least 10 Å away from any of the DNA atoms. Na⁺ ions treated using the Joung–Cheatham parameters were then added to neutralize the charge of the system. The system was then energy minimized in two stages with the solute heavy atoms (except for the atoms comprising the m⁶2A...U bp and the m⁶(*syn*)A...U bp) being fixed (with a restraint of 500 kcal/mol/Å²)

during the first stage. Heating, equilibration, and production runs (500 ns) were performed as described previously⁷¹. To maintain the methyl group in the *syn* conformation during the MD simulation of the dsGGACU duplex with the m⁶(*syn*) A...U bp, a torsion angle restraint was applied on the angle spanning the methyl carbon-N6-C6-C5 atoms of m⁶A. The restraint was chosen to be square wellled between 160° and 200°, parabolic between 159–160° and 200–201°, and linear beyond 201° and <159°, with a force constant of 32 kcal/mol/Å². Force field parameters for m⁶A were derived from those by Aduri et al.⁷². In particular, the atom types and charges for the methyl group were taken from those by Aduri et al., while retaining atom types and charges (apart from N6, see below) for the remaining atoms from those of adenine in the AMBER ff99bsc0 χ_{OL3} force field. Charges on the amino N6 atom of m⁶A were adjusted to maintain a net charge for the m⁶A nucleoside of –1. An analogous procedure was followed to generate the parameters for the m⁶2A nucleoside. Missing force field parameters were generated using the *antechamber* and *parmchk* utilities of the AMBER suite (16.0). All the structure visualization was performed in PyMOL (<https://pymol.org/>).

Automated fragmentation quantum mechanics/molecular mechanics

chemical-shift calculations. We generated mono-nucleoside models of m⁶A with the N1-C6-N6-methyl carbon dihedral angle ranging from 0° to 360° in steps of 20° (*syn* conformation is 0°, whereas *anti* conformation is 180°). Coordinates of the m⁶A residue were derived from Aduri et al.⁷². We subjected the various mono-nucleoside models and all the RNA duplex MD ensembles (each with $N = 100$) to QM/MM chemical-shift calculations using a fragmentation procedure as described previously⁷³. The parameters of geometric minimization for RNA structures were described in a prior study⁷⁴. For all the RNA duplex ensembles, the chemical-shift calculations were solely focused on A6 and U13 residues in dsGGACU; therefore, each conformer in the RNA duplex ensembles was broken into only two quantum fragments centered on A6 or U13, respectively, whereas for all the mono-nucleoside models, each quantum fragment was the single mono-nucleoside. We then used a distribution of point charges on the fragment surface to represent the effects of RNA that is outside the quantum fragment and solvent⁷⁵. The local dielectric ϵ value was set to be 1, 4, and 80 for RNA inside the quantum fragment, RNA outside the quantum fragment, and RNA outside the solvent, respectively. We then performed the GIAO chemical-shift calculations for each quantum fragment with the OLYP functional and the pcSseg-0 basis set, using demon-2k program (http://www.demon-software.com/public_html/download.html). Reference shieldings were computed for TMS and nitromethane at the same level of theory.

Free energy decomposition along the CS pathway. The free energy of annealing the methylated duplex can be decomposed into two steps (CS pathway):

$$\text{Step 1 : } ssRNA^{syn} \rightleftharpoons ssRNA^{anti} \quad (12)$$

$$\text{Step 2 : } ssRNA^{anti} + ss2 \rightleftharpoons dsRNA^{anti} \quad (13)$$

k_1 and k_{-1} were determined from two-state fits or temperature dependence of the RD data (see ‘‘Determining the methylamino isomerization rate constants from temperature-dependent RD measurements for methylated ssRNA and dsRNA’’ section above):

$$\Delta G_{iso,ss}^\circ = -RT \ln\left(\frac{k_1}{k_{-1}}\right) \quad (14)$$

The apparent free energy of annealing methylated dsRNA was determined using:

$$\Delta G_{anneal,m^6A}^{\circ,app} = -RT \ln\left(\frac{[ssRNA^{syn}][ss2]}{[dsRNA^{anti}]}\right) \quad (15)$$

in which the concentrations of the relevant species were measured based on two-state fits of the RD data²¹:

$$[ssRNA^{anti}] = \frac{[ssRNA^{total}] \times k_1}{k_1 + k_{-1}} \quad (16)$$

$$[ssRNA^{syn}] = \frac{[ssRNA^{total}] \times k_{-1}}{k_1 + k_{-1}} \quad (17)$$

$$[ssRNA^{total}] = C_t \times p_{ss} \quad (18)$$

$$[dsRNA^{anti}] = C_t \times p_{GS} \quad (19)$$

$$[ss2] = [ss2]_{total} - [dsRNA^{anti}] - [dsRNA^{syn}] \quad (20)$$

$$[dsRNA^{syn}] = C_t \times p_{ES} \quad (21)$$

p_{ss} and p_{GS} are the populations of the ssRNA^{total} ($ssRNA^{syn} + ssRNA^{anti}$) and dsRNA^{anti} species obtained from the RD data. [ss2]_{total} is the total complementary strand concentration. Note that at $T = 65$ °C, dsRNA^{syn} has a negligible contribution to RD profiles ([dsRNA^{anti}] = 0), while at $T = 55$ °C, dsRNA^{syn} population (p_{ES}) was obtained from a three-state fit of the m⁶A–C2 CEST data for dsGGACU^{m⁶A}. Also

note that the $\Delta G_{\text{anneal},m^6A}^{\text{app}}$ here differs slightly (by ~ 0.1 kcal/mol) from the prior study²¹, where ssRNA^{syn} and ssRNA^{anti} were not distinguished.

The free energy of annealing ssRNA^{anti} is given by:

$$\Delta G_{\text{anneal},\text{anti}}^{\circ} = \Delta G_{\text{anneal},m^6A}^{\text{app}} - \Delta G_{\text{iso},\text{ss}}^{\circ} \quad (22)$$

$$k_{\text{off},\text{anti}} = \frac{k_{\text{on},\text{anti}}}{e^{\frac{\Delta G_{\text{anneal},\text{anti}}^{\circ}}{-RT}}} \quad (23)$$

$$\Delta \Delta G_{\text{anneal},\text{anti}}^{\circ} = \Delta G_{\text{anneal},\text{anti}}^{\circ} - \Delta G_{\text{anneal},A}^{\circ} \quad (24)$$

At $T = 55^{\circ}\text{C}$, $\Delta \Delta G_{\text{anneal},\text{anti}}^{\circ} = 0.5 \pm 0.2$ kcal/mol, and the m⁶A methyl group in anti conformation slightly destabilizes the duplex, whereas it stabilized it by a comparable amount at $T = 65^{\circ}\text{C}$ ($\Delta \Delta G_{\text{anneal},\text{anti}}^{\circ} = -0.5 \pm 0.2$ kcal/mol).

B-M simulations and constrained fits. When dealing with three- or four-state exchange, there is always a danger of overfitting the RD data. For this reason, we initially performed simulations in which all of the relevant kinetic rate constants, populations, $\Delta\omega$, R_1 , and R_2 of the different species were approximated to values measured experimentally using the appropriate RNA constructs (Supplementary Figs. 2b and 6a and Supplementary Table 1). These values were then used in a three- or four-state simulation to simulate CEST profiles without any adjustable parameters. We then performed constrained fits in which the parameters (population, rate constants, $\Delta\omega$, R_1 , and R_2) were allowed to float by an amount determined by the experimentally measured uncertainty (1 s.d.).

The simulations and constrained fits were performed by numerically integrating the appropriate B-M equations³⁴. Briefly, the simulations were performed by directly predicting RD profiles for a given set of exchange parameters that are defined below. In the constrained fitting, the same numerical integration was used to fit exchange parameters applying specific constraints as detailed below.

Three-state CS simulations and constrained fits for the dsA6DNA^{m6A} RD data measured at T = 65 °C. These analyses used the following input exchange parameters:

1. k_1 and k_{-1} were obtained from the temperature-dependent RD measurements on ssGGACU^{m6A} (Supplementary Fig. 2c).
2. $k_{\text{off},\text{anti}}$ was assumed equal to k_{off} measured for the unmethylated dsGGACU and $k_{\text{on},\text{anti}}$ was obtained from the energetic decomposition described above (Eq. 23).
3. The longitudinal (R_1) and transverse (R_2) relaxation rate constants for all three species (ssRNA^{syn}, ssRNA^{anti}, and dsRNA^{anti}) were obtained from two-state fits of the CEST RD data probing duplex melting at $T = 65^{\circ}\text{C}$ ²¹. $R_1(\text{ssRNA}^{\text{anti}}) = R_1(\text{ssRNA}^{\text{syn}}) = R_1(\text{dsRNA}^{\text{anti}}) = R_{1,\text{GS}} = R_{1,\text{ES}}$. $R_2(\text{ssRNA}^{\text{anti}}) = R_2(\text{ssRNA}^{\text{syn}}) = R_{2,\text{ES}}$. $R_2(\text{dsRNA}^{\text{anti}}) = R_{2,\text{GS}}$.
4. The equilibrium populations $P(\text{ssRNA}^{\text{syn}})$, $P(\text{ssRNA}^{\text{anti}})$, and $P(\text{dsRNA}^{\text{anti}})$ were obtained from kinetic simulations (see differential equations below) that were sufficiently long to ensure equilibration. The same equilibrium populations were obtained from analytical expressions outlined in ref. 76:

$$\frac{d[\text{ssRNA}^{\text{syn}}]}{dt} = -k_1[\text{ssRNA}^{\text{syn}}] + k_{-1}[\text{ssRNA}^{\text{anti}}] \quad (25)$$

$$\frac{d[\text{ssRNA}^{\text{anti}}]}{dt} = k_1[\text{ssRNA}^{\text{syn}}] - k_{-1}[\text{ssRNA}^{\text{anti}}] - k_{\text{on},\text{anti}}[\text{ssRNA}^{\text{anti}}][\text{ss2}] + k_{\text{off},\text{anti}}[\text{dsRNA}^{\text{anti}}] \quad (26)$$

$$\frac{d[\text{dsRNA}^{\text{anti}}]}{dt} = k_{\text{on},\text{anti}}[\text{ssRNA}^{\text{anti}}][\text{ss2}] - k_{\text{off},\text{anti}}[\text{dsRNA}^{\text{anti}}] \quad (27)$$

$$\frac{d[\text{ss2}]}{dt} = -k_{\text{on},\text{anti}}[\text{ssRNA}^{\text{anti}}][\text{ss2}] + k_{\text{off},\text{anti}}[\text{dsRNA}^{\text{anti}}] \quad (28)$$

5. $\Delta\omega$ of ssRNA^{syn} and ssRNA^{anti} for C2: $\Delta\omega_{\text{ss},\text{syn}} = \omega_{\text{ss},\text{syn}} - \omega_{\text{ds},\text{anti}}$, in which $\omega_{\text{ss},\text{syn}} = \omega_{\text{ss}} - \frac{P(\text{ssRNA}^{\text{syn}})}{P(\text{ssRNA}^{\text{syn}}) + P(\text{ssRNA}^{\text{anti}})} \times \Delta\omega_{\text{ss},\text{anti-syn}}$. $\Delta\omega_{\text{ss},\text{anti}} = \omega_{\text{ss},\text{anti}} - \omega_{\text{ds},\text{anti}}$, in which $\omega_{\text{ss},\text{anti}} = \omega_{\text{ss}} + \frac{P(\text{ssRNA}^{\text{anti}})}{P(\text{ssRNA}^{\text{syn}}) + P(\text{ssRNA}^{\text{anti}})} \times \Delta\omega_{\text{ss},\text{anti-syn}}$. ω_{ss} and $\omega_{\text{ds},\text{anti}}$ were obtained from 2D HSQC spectra (Supplementary Fig. 1) and $\Delta\omega_{\text{ss},\text{anti-syn}}$ was obtained from ssGGACU^{m6A} RD measurements at $T = 25^{\circ}\text{C}$ and was assumed to be temperature independent, as supported by the data collected in this study (Supplementary Fig. 2, Supplementary Table 1). Since C8 is not sensitive to methylamino isomerization (Supplementary Fig. 2), $\Delta\omega_{\text{ss},\text{anti}} = 0$, while $\Delta\omega_{\text{ss},\text{syn}}$ is obtained from the two-state fit of the CEST RD data probing duplex melting at $T = 65^{\circ}\text{C}$ ²¹.

The above parameters were fixed to simulate the CEST profiles using a three-state B-M equation³⁴. For the constrained three-state fit, the ratio (but not absolute magnitude) of $k_{\text{on},\text{anti}}$ to $k_{\text{off},\text{anti}}$ was constrained to preserve the free energy of the hybridization step. All other parameters (population, k_1 , k_{-1} , $\Delta\omega$, R_1 , and R_2 for all

species) were allowed to float by an amount determined by the uncertainty (1 s.d.). When possible, global constrained three-state B-M fits were carried out on both m⁶A C8 and C2 CEST data (Fig. 2f). χ_{red}^2 was calculated to assess the goodness of fitting¹⁸.

Three-state IF simulations and constrained fits for the dsGGACU^{m6A} RD data were measured at T = 65 and 55 °C. These analyses used the following input exchange parameters:

1. k_2 , k_{-2} , $k_{\text{on},\text{syn}}$, $k_{\text{off},\text{syn}}$, C2 $\Delta\omega_{\text{ds},\text{syn}}$, C2 $R_1(\text{dsRNA}^{\text{syn}}) = R_1(\text{dsRNA}^{\text{anti}}) = R_{1,\text{GS}}$, and $R_2(\text{dsRNA}^{\text{syn}}) = R_2(\text{dsRNA}^{\text{anti}}) = R_{2,\text{GS}}$ were obtained from a three-state fit to the dsGGACU^{m6A} m⁶A-C2 RD data (Fig. 3a and Supplementary Table 3) using the triangular topology at $T = 55^{\circ}\text{C}$ or from RD measurements done on the hairpin constructs at $T = 65^{\circ}\text{C}$ (Supplementary Fig. 6a). C8 $\Delta\omega_{\text{ds},\text{syn}} = 0$ because C8 is not sensitive to methylamino isomerization (Supplementary Fig. 6a). C8 $R_1(\text{dsRNA}^{\text{syn}}) = R_1(\text{dsRNA}^{\text{anti}}) = R_{1,\text{GS}}$, and $R_2(\text{dsRNA}^{\text{syn}}) = R_2(\text{dsRNA}^{\text{anti}}) = R_{2,\text{GS}}$ were obtained from a two-state fit to the dsGGACU^{m6A} m⁶A-C8 RD data (Supplementary Table 1), $\Delta\omega_{\text{ss},\text{syn}}$ is obtained from the two-state fit of the CEST RD data probing duplex melting at $T = 65$ and 55°C ²¹.
2. The equilibrium populations $P(\text{ssRNA}^{\text{syn}})$, $P(\text{dsRNA}^{\text{syn}})$, $P(\text{dsRNA}^{\text{anti}})$ were obtained from kinetic simulations (see differential equations below) that were sufficiently long to ensure equilibration:

$$\frac{d[\text{ssRNA}^{\text{syn}}]}{dt} = k_{\text{off},\text{syn}}[\text{dsRNA}^{\text{syn}}] - k_{\text{on},\text{syn}}[\text{ssRNA}^{\text{syn}}][\text{ss2}] \quad (29)$$

$$\frac{d[\text{dsRNA}^{\text{syn}}]}{dt} = -k_{\text{off},\text{syn}}[\text{dsRNA}^{\text{syn}}] + k_{\text{on},\text{syn}}[\text{ssRNA}^{\text{syn}}][\text{ss2}] + k_2[\text{dsRNA}^{\text{anti}}] - k_{-2}[\text{dsRNA}^{\text{syn}}] \quad (30)$$

$$\frac{d[\text{dsRNA}^{\text{anti}}]}{dt} = k_{-2}[\text{dsRNA}^{\text{syn}}] - k_2[\text{dsRNA}^{\text{anti}}] \quad (31)$$

$$\frac{d[\text{ss2}]}{dt} = k_{\text{off},\text{syn}}[\text{dsRNA}^{\text{syn}}] - k_{\text{on},\text{syn}}[\text{ssRNA}^{\text{syn}}][\text{ss2}] + k_{\text{off},\text{anti}}[\text{dsRNA}^{\text{anti}}] \quad (32)$$

The same approach was used to simulate/fit CEST profiles for the IF pathway as described in the previous section.

Four-state CS + IF simulations and constrained fits for the dsGGACU^{m6A} RD data at T = 55 °C. These analyses used the following input exchange parameters:

1. All of the exchange parameters related to the CS pathway (k_1 , k_{-1} , $k_{\text{on},\text{anti}}$, $k_{\text{off},\text{anti}}$, $\Delta\omega_{\text{ss},\text{syn}}$, $\Delta\omega_{\text{ss},\text{anti}}$, $R_1(\text{ssRNA}^{\text{anti}})$, $R_1(\text{ssRNA}^{\text{syn}})$, $R_1(\text{dsRNA}^{\text{anti}})$, $R_2(\text{ssRNA}^{\text{anti}})$, $R_2(\text{ssRNA}^{\text{syn}})$, and $R_2(\text{dsRNA}^{\text{anti}})$) and the IF pathway (k_{-2} , k_2 , $k_{\text{on},\text{syn}}$, $k_{\text{off},\text{syn}}$, $R_1(\text{dsRNA}^{\text{syn}})$, and $\Delta\omega_{\text{ds},\text{syn}}$) were obtained as described in the previous sections for the three-state CS and IF analysis, respectively.
2. The population of all four species was obtained from four-state kinetic simulations using the eight rate constants (k_1 , k_{-1} , $k_{\text{on},\text{anti}}$, $k_{\text{off},\text{anti}}$, k_{-2} , k_2 , $k_{\text{on},\text{syn}}$, $k_{\text{off},\text{syn}}$) based on the CS + IF model (see differential equations below). The same equilibrium populations were obtained from analytical expressions outlined in ref. 76:

$$\frac{d[\text{ssRNA}^{\text{syn}}]}{dt} = -k_1[\text{ssRNA}^{\text{syn}}] + k_{-1}[\text{ssRNA}^{\text{anti}}] + k_{\text{off},\text{syn}}[\text{dsRNA}^{\text{syn}}] - k_{\text{on},\text{syn}}[\text{ssRNA}^{\text{syn}}][\text{ss2}] \quad (33)$$

$$\frac{d[\text{ssRNA}^{\text{anti}}]}{dt} = k_1[\text{ssRNA}^{\text{syn}}] - k_{-1}[\text{ssRNA}^{\text{anti}}] - k_{\text{on},\text{anti}}[\text{ssRNA}^{\text{anti}}][\text{ss2}] + k_{\text{off},\text{anti}}[\text{dsRNA}^{\text{anti}}] \quad (34)$$

$$\frac{d[\text{dsRNA}^{\text{syn}}]}{dt} = -k_{\text{off},\text{syn}}[\text{dsRNA}^{\text{syn}}] + k_{\text{on},\text{syn}}[\text{ssRNA}^{\text{syn}}][\text{ss2}] + k_2[\text{dsRNA}^{\text{anti}}] - k_{-2}[\text{dsRNA}^{\text{syn}}] \quad (35)$$

$$\frac{d[\text{dsRNA}^{\text{anti}}]}{dt} = k_{\text{on},\text{anti}}[\text{ssRNA}^{\text{anti}}][\text{ss2}] - k_{\text{off},\text{anti}}[\text{dsRNA}^{\text{anti}}] + k_{-2}[\text{dsRNA}^{\text{syn}}] - k_2[\text{dsRNA}^{\text{anti}}] \quad (36)$$

$$\frac{d[\text{ss2}]}{dt} = k_{\text{off},\text{syn}}[\text{dsRNA}^{\text{syn}}] - k_{\text{on},\text{syn}}[\text{ssRNA}^{\text{syn}}][\text{ss2}] - k_{\text{on},\text{anti}}[\text{ssRNA}^{\text{anti}}][\text{ss2}] + k_{\text{off},\text{anti}}[\text{dsRNA}^{\text{anti}}] \quad (37)$$

The exchange parameters described above were then used to simulate the CEST profile using the four-state B–M equation (see below)⁶²:

$$\frac{d}{dt} \begin{pmatrix} I_{GSx} \\ I_{GSy} \\ I_{GSz} \\ I_{ES1x} \\ I_{ES1y} \\ I_{ES1z} \\ I_{ES2x} \\ I_{ES2y} \\ I_{ES2z} \\ I_{ES3x} \\ I_{ES3y} \\ I_{ES3z} \end{pmatrix} = \begin{pmatrix} -R_{2,GS} - k_{12} - k_{54} & -\Omega_{GS} & \omega & k_{21} & 0 & 0 & 0 & 0 & 0 & 0 & 0 & 0 \\ \Omega_{GS} & -R_{2,GS} - k_{12} - k_{54} & 0 & 0 & k_{21} & 0 & 0 & 0 & 0 & 0 & 0 & 0 \\ -\omega & 0 & -R_{1,ES} - k_{12} - k_{54} & 0 & 0 & k_{21} & 0 & 0 & 0 & 0 & 0 & 0 \\ k_{12} & 0 & 0 & -R_{2,ES1} - k_{23} - k_{21} & -\Omega_{ES1} & \omega & k_{32} & 0 & 0 & 0 & 0 & 0 \\ 0 & k_{12} & 0 & 0 & \Omega_{ES1} & -\omega & 0 & 0 & 0 & 0 & 0 & 0 \\ 0 & 0 & 0 & 0 & -\omega & 0 & 0 & -R_{1,ES1} - k_{23} - k_{21} & 0 & 0 & 0 & 0 \\ 0 & 0 & 0 & 0 & 0 & k_{23} & 0 & 0 & -R_{2,ES2} - k_{32} - k_{34} & -\Omega_{ES2} & \omega & 0 \\ 0 & 0 & 0 & 0 & 0 & 0 & k_{32} & 0 & -\Omega_{ES2} & -\omega & 0 & 0 \\ 0 & 0 & 0 & 0 & 0 & 0 & 0 & k_{33} & 0 & 0 & 0 & 0 \\ 0 & 0 & 0 & 0 & 0 & 0 & 0 & 0 & 0 & 0 & 0 & 0 \\ k_{54} & 0 & 0 & 0 & 0 & 0 & 0 & 0 & 0 & 0 & -R_{2,ES3} - k_{43} - k_{45} & 0 \\ 0 & k_{54} & 0 & 0 & 0 & 0 & 0 & k_{34} & 0 & \Omega_{ES3} & -R_{2,ES3} - k_{43} - k_{45} & 0 \\ 0 & 0 & 0 & 0 & 0 & 0 & 0 & 0 & k_{34} & 0 & 0 & -\Omega_{ES3} \\ 0 & 0 & k_{54} & 0 & 0 & 0 & 0 & 0 & 0 & k_{34} & -\omega & -R_{1,ES3} - k_{43} - k_{45} \end{pmatrix} \begin{pmatrix} I_{GSx} \\ I_{GSy} \\ I_{GSz} \\ I_{ES1x} \\ I_{ES1y} \\ I_{ES1z} \\ I_{ES2x} \\ I_{ES2y} \\ I_{ES2z} \\ I_{ES3x} \\ I_{ES3y} \\ I_{ES3z} \end{pmatrix} + \begin{pmatrix} 0 \\ 0 \\ R_{1,GS} I_{GSz,eq} \\ 0 \\ 0 \\ R_{1,ES1} I_{ES1z,eq} \\ 0 \\ 0 \\ R_{1,ES2} I_{ES2z,eq} \\ 0 \\ 0 \\ R_{1,ES3} I_{ES3z,eq} \end{pmatrix} \quad (38)$$

{GS/ES_i}_{x/y/z} (*i* = 1, 2, 3) denotes the magnetization of the GS or ESs in the specified direction. $R_{2,GS}$, $R_{2,ES1}$, $R_{2,ES2}$, and $R_{2,ES3}$ are the transverse relaxation rate constants for the GS (dsRNA^{anti}), ES1 (dsRNA^{syn}), ES2 (ssRNA^{syn}), and ES3 (ssRNA^{anti}), respectively. $R_{1,GS}$, $R_{1,ES1}$, $R_{1,ES2}$, and $R_{1,ES3}$ are corresponding longitudinal relaxation rate constants. ω is the RF field power; $k_{i(j)}$ and $k_{(j)i}$ are the forward and backward rate constants of reactions shown in Fig. 5a. Specifically, $k_{12} = k_2$, and $k_{21} = k_{-2}$ are the forward and backward rate constants of methylamino isomerization in dsRNA. $k_{23} = k_{off, syn}$, $k_{32} = k_{on, syn}$ [ss2]. $k_{34} = k_1$ and $k_{43} = k_{-1}$ are the forward and backward rate constants of methylamino isomerization in ssRNA. $k_{45} = k_{on, anti}$ [ss2] and $k_{54} = k_{off, anti}$. $I_{i(GS/ES)_z, eq}$ (*i* = 1, 2, 3) denotes the longitudinal magnetization of the GS or ESs at the start of the experiment. ω_i (*i* = 1, 2, 3, 4) are the offset frequencies of the GS, or ES resonances in the rotating frame of the RF field⁶¹.

We carried out two independent constrained four-state fits at $T = 55^\circ\text{C}$ that differ with regards to how $k_{on, syn}$ and $k_{off, syn}$ were defined. In one case, $k_{on, syn}$ was assumed to be equal to the $k_{ss \rightarrow ES}$ rate constant obtained from a three-state fit to the CEST data measured for dsGGACU^{m6A} at $T = 55^\circ\text{C}$ (Fig. 3b) using the triangular topology. Note that this is an approximation since the ssRNA represents the major ssRNA^{syn} and minor ssRNA^{anti} species in fast exchange. $k_{off, syn}$ was then calculated by closing the thermodynamic cycle:

$$\Delta G_{anneal, syn}^\circ = \Delta G_{anneal, m6A}^{\circ, app} - \Delta G_{iso, ds}^\circ \quad (39)$$

$$\Delta G_{iso, ds}^\circ = -RT \ln \left(\frac{k_{-2}}{k_2} \right) \quad (40)$$

$$k_{off, syn} = \frac{k_{on, syn}}{e^{\frac{\Delta G_{anneal, syn}^\circ}{-RT}}} \quad (41)$$

All other exchange parameters were then allowed to float by an amount determined by the experimental uncertainty (one standard deviation). In the second case, only the ratio (but not absolute magnitude) of $k_{on, syn}$ to $k_{off, syn}$ was constrained to preserve the free energy of the hybridization step. The fitted $k_{on, syn}$ and $k_{off, syn}$ values were similar using these two independent methods. The results from the second method were reported in Fig. 5a and Supplementary Table 2. When possible, global constrained four-state B–M fits were carried out on both m^{6A} C8 and C2 CEST data. χ^2_{red} was calculated to assess the goodness of fitting¹⁸.

Four-state constrained fits for the CS + IF model for dsGGACU^{m6A} at $T = 65^\circ\text{C}$. Because the dsRNA^{syn} ES was not directly detected at $T = 65^\circ\text{C}$, the RD data were analyzed as described for $T = 55^\circ\text{C}$, with the exception that k_2 and k_{-2} were measured in hpGGACU^{m6A} at $T = 65^\circ\text{C}$ using R_{1p} RD (Supplementary Fig. 6a), $k_{on, syn}$ was assumed to be equal to $k_{on}/20$. This 20-fold slowdown in annealing of ssRNA^{syn} relative to unmethylated ssRNA was observed for dsGGACU^{m6A} at $T = 55^\circ\text{C}$. $k_{off, syn}$ was then calculated by closing the thermodynamic cycle (Eq. 37). Similar results were obtained when assuming $k_{off, syn}$ is equal to $k_{off} \times 80$ as observed for dsGGACU^{m6A} at $T = 55^\circ\text{C}$, and closing the cycle (Eq. 37) to calculate $k_{on, syn}$.

Four-state constrained fits for the CS + IF model for dsHCVm^{6A} and dsA6DNA^{m6A}. RD data measured for dsHCVm^{6A} and dsA6DNA^{m6A} were analyzed in a similar manner as described in the previous sections.

- k_1 , k_{-1} and k_2 , k_{-2} were assumed to be the same as those measured in GGACU^{m6A} constructs using temperature-dependent RD measurements (Supplementary Figs. 2c and 6d).
- R_1 (ssRNA^{anti}) = R_1 (ssRNA^{syn}) = R_1 (dsRNA^{anti}) = $R_{1,GS} = R_{1,ES}$. R_2 (ssRNA^{anti}) = R_2 (ssRNA^{syn}) = $R_{2,ES}$. R_2 (dsRNA^{anti}) = $R_{2,GS}$. $R_{1,ES}$ and $R_{2,GS}$ were obtained from a two-state fit to the RD data probing duplex melting (Supplementary Table 1).
- $\Delta\omega_{ss, anti} = \Delta\omega_{ds, syn} = 0$ for A11–C8 in dsHCVm^{6A} since A11 is not the m^{6A} site. $\Delta\omega_{ss, syn}$ was assumed to be equal to the $\Delta\omega$ value for A11–C8 in ssRNA obtained from a two-state fit of the A11–C8 RD data²¹.
- $\Delta\omega_{ss, syn}$ and $\Delta\omega_{ss, anti}$ for m^{6A}16–C2 in dsA6DNA^{m6A} were determined as described in CS three-state simulation for dsGGACU^{m6A} at $T = 65^\circ\text{C}$, assuming $\Delta\omega_{ss, anti-syn}$ of ssA6DNA^{m6A} is the same as that of ssGGACU^{m6A}. $\Delta\omega_{ds, syn}$ was assumed to be equal to that measured for hpGGACU^{m6A} at $T = 55^\circ\text{C}$ (Supplementary Table 1).

Flux calculations. Flux through the CS (F_{CS}) and IF (F_{IF}) pathways was calculated as the harmonic mean of the forward rates along the CS and IF pathways²⁷:

$$F_{CS} = \left(\frac{1}{k_1 [ssRNA^{syn}]} + \frac{1}{k_{on, anti} [ssRNA^{anti}] [ss2]} \right)^{-1} \quad (42)$$

$$F_{IF} = \left(\frac{1}{k_{on, syn} [ssRNA^{syn}] [ss2]} + \frac{1}{k_{-2} [dsRNA^{syn}]} \right)^{-1} \quad (43)$$

All concentrations are equilibrium concentrations obtained using constrained four-state fit of CEST data (Fig. 5c) or CS + IF kinetic modeling.

Model to predict apparent k_{on} and k_{off} for methylated RNA/DNA duplexes and TAR. The four-state CS + IF model was used to simulate time traces describing the evolution of all four species as a function of time starting from 100% ssRNA^{syn} at $t = 0$. Similar results were obtained when performing simulations starting with an equilibrium population of ssRNA^{syn} ($k_{-1}/(k_1 + k_{-1})$) and ssRNA^{anti} ($k_1/(k_1 + k_{-1})$). k_1 , k_{-1} , k_{-2} , and k_2 were all assumed equal to the corresponding values measured for ssGGACU^{m6A} and dsGGACU^{m6A} at the appropriate temperature based on the temperature-dependent RD measurements (Supplementary Figs. 2c and 6d). $k_{off, anti}$ was assumed to be equal to k_{off} , and $k_{on, anti}$ was deduced from closing the thermodynamic cycle (Eq. 23). $k_{on, syn}$ and $k_{off, syn}$ were obtained using two different approaches and yielded similar predictions for the apparent k_{on} and k_{off} for methylated RNA/DNA duplexes and TAR. In one case, $k_{on, syn} = k_{on}/20$ and $k_{off, syn}$ was deduced from closing the thermodynamic cycle (Eq. 37). Alternatively, $k_{off, syn} = k_{off} \times 80$ and $k_{on, syn}$ was deduced from closing the thermodynamic cycle (Eq. 37). The predictions shown in Fig. 6a

were obtained using the former approach. $k_{\text{on},m^6A}^{\text{app}}$ and $k_{\text{off},m^6A}^{\text{app}}$ were obtained by fitting simulated time course of $[\text{dsRNA}^{\text{syn}}] + [\text{dsRNA}^{\text{anti}}]$ at multiple time points to numerical solutions of Eqs. (40) and (41) for a two-state hybridization model $\text{ss1} + \text{ss2} \Delta\text{s}$, $k_{\text{on},m^6A}^{\text{app}}$ and $k_{\text{off},m^6A}^{\text{app}}$ are the annealing and melting constants, respectively:

$$\frac{d[\text{ds}]}{dt} = k_{\text{on},m^6A}^{\text{app}}[\text{ss1}][\text{ss2}] - k_{\text{off},m^6A}^{\text{app}}[\text{ds}] \quad (44)$$

$$\frac{d[\text{ss1}]}{dt} = \frac{d[\text{ss2}]}{dt} = -k_{\text{on},m^6A}^{\text{app}}[\text{ss1}][\text{ss2}] + k_{\text{off},m^6A}^{\text{app}}[\text{ds}] \quad (45)$$

Similar results were obtained when fitting simulated time course of $[\text{dsRNA}^{\text{anti}}]$ only. However, it should be noted that for certain kinetic regimes outside those examined here, particularly when $k_{\text{on},\text{syn}}$ is ultra-fast, there can be a substantial accumulation of the $\text{dsRNA}^{\text{syn}}$. In this scenario, the system is poorly defined with the apparent two-state approximation and separate rate constants are needed to describe the evolution of all species. In addition, similar results were obtained from fitting the traces to the appropriate two-state second-order kinetic equation (see ref. 77). Finally, similar results were obtained when simulating m^6A -C8 RD profiles using the four-state CS + IF model together with exchange parameters ($\Delta\omega$, R_1 , and R_2 values for all species) derived from the dsGACU^{m^6A} 55 °C m^6A -C8 CEST data, and then fitting the data to a two-state model. Note that C8 was used the probe instead of C2 because the two-state fit results vary depending on the three $\Delta\omega$ values used in the C2 CEST simulation. On the other hand, varying the one $\Delta\omega$ value used in the C8 CEST simulation does not affect the two-state fit results. As the choice of exchange parameters (R_1 and R_2 values) had a minor effect on the two-state fit results, we show results from the kinetic simulations in Fig. 6a and that from the two-state fitting to the simulated C8 RD data in Supplementary Fig. 9b.

A similar approach was used to compute the apparent k_{forward} and k_{backward} rate constants for methylated TAR, except that k_1 , k_{-1} were assumed to be equal to the values measured for m^6A AMP, which is a better mimic of the environment of the flipped out and unstacked A35 in TAR than ssRNA. Apparent k_{forward} and k_{backward} rate constants were obtained by fitting simulated time course of $[\text{ES}]$ at multiple time points to the equation $[\text{ES}] = A(1 - e^{-k_{\text{ext}}t})$, where A is a pre-exponential factor. Note that for the energetics decomposition and kinetic simulations of TAR, the $[\text{ss2}]$ term in all equations above was removed since the TAR conformational transition is a first-order reaction.

Predict m^6A -induced slowdown of DNA hybridization in the mouse genome.

We used our four-state CS + IF model to predict the hybridization kinetics for 12-mer DNA duplex representing 5951 m^6A sites in the mouse genome⁹, in which m^6A was positioned at the sixth nucleotide. k_{on} of unmethylated DNA was predicted as described previously⁴⁵ (<http://nablab.rice.edu/nabtools/kinetics.html>). The free energy ($\Delta G_{\text{anneal},A}^{\circ}$) of each sequence was predicted using the MELTING program (<https://www.ebi.ac.uk/biomodels-static/tools/melting/>). $k_{\text{off}} = \frac{k_{\text{on}}}{e^{\frac{\Delta G_{\text{anneal},A}^{\circ}}{RT}}}$. In all cases,

the thermodynamic destabilization of the duplex by m^6A ($\Delta\Delta G_{\text{anneal},m^6A}^{\circ}$) was assumed to be 1 kcal/mol based on prior studies^{12,78} and our measurements (Supplementary Table 4). $\Delta G_{\text{anneal},m^6A}^{\circ\text{app}}$ was obtained from $\Delta G_{\text{anneal},m^6A}^{\circ} + \Delta\Delta G_{\text{anneal},m^6A}^{\circ}$. $k_{\text{on}}^{\text{app}}$, $k_{\text{off}}^{\text{app}}$, and $\Delta G_{\text{anneal},m^6A}^{\circ\text{app}}$ were then used as inputs to predict $k_{\text{on},m^6A}^{\text{app}}$ and $k_{\text{off},m^6A}^{\text{app}}$ as described in the previous sections. The concentration of dsDNA was assumed to be 1 mM and $T = 37$ °C. We also used this approach to predict the impact of m^6A on RNA hybridization kinetics at $T = 37$ °C using rate constants for hybridization of unmethylated RNA reported previously²² at $T = 37$ °C and assuming that m^6A destabilizes dsRNA by 1 kcal/mol¹². m^6A was predicted to slow k_{on} by ~5-fold while having a minor effect (<2-fold) on k_{off} , consistent with our measurements at higher temperatures.

Survey of single H-bonded A-U bps in PDB structures.

To identify singly H-bonded A-U bp conformations that mimic the $m^6(\text{syn})A \cdots U$ ES, we conducted a structural survey of the RCSB PDB⁷⁹. All X-ray (with resolution ≤ 3.0 Å) and NMR biological assemblies containing RNA molecules (including naked RNA, RNA protein complex, etc.) were downloaded from RCSB PDB on Aug 2017 and processed by X3DNA-DSSR⁸⁰ to generate a searchable database containing RNA structural information. Potential candidates of single H-bonded A-U bp were identified by applying the following filters in the database: (1) A-U bps are unmethylated; (2) the Leontis–Westhof (LW) classification⁸¹ is “cWW””; (3) both A and U are not in *syn* conformation at glycosidic bond; (4) A-U bps contain A(N1)–U(N3) H-bond (distance between A(N1) and U(N3) is <3.5 Å) but do not contain A(N6)–U(O4) H-bond (distance between A(N6) and U(O4) is >3.5 Å). We then manually inspected all the single H-bonded A-U bps, removed misregistered bps, and classified the structure context of all the resulting bps into the following categories (Supplementary Fig. 7e):

1. Junction: A-U bp that is next to an internal bulge, a mismatch or an apical loop.
2. Junction-1/2/3: 1/2/3 bp away from the junction.
3. Tertiary: involved in tertiary interactions.

4. Terminal: at terminal ends.
5. Terminal-1/2/3: 1/2/3 bp away from the terminal end.
6. Duplex: A-U bp at the canonical duplex context

Reporting summary. Further information on research design is available in the Nature Research Reporting Summary linked to this article.

Data availability

The data supporting the findings of this study are available from the corresponding authors upon reasonable request. The NMR $R_{1\rho}$ (Fig. 2c and Supplementary Figs. 2a, b, 5, 6a, and 10b, c, d), CEST (Figs. 2c, f, 3a, c, 4b–d, and 5b and Supplementary Figs. 2b, 3a–c, 4a, c–e, 5, 6a, and 9a, d) and imino exchange (Supplementary Fig. 8c, d) data as well as kinetic simulation and prediction results (Fig. 6a and Supplementary Fig. 9b) generated in this study are provided at https://github.com/alhashimilab/m6A_hybridization_kinetics (<https://doi.org/10.5281/zenodo.5106694>)⁸². The force field parameters for m^6A and m^6A used in MD simulations and PDB files of these structures that were submitted to the DFT calculations (Fig. 4g and Supplementary Fig. 7c) are provided at https://github.com/alhashimilab/m6A_ES (<https://doi.org/10.5281/zenodo.5099581>)⁸³. The results of PDB (RCSB Protein Data Bank) survey for singly H-bond A-U bps (Supplementary Fig. 7f) are provided at https://github.com/alhashimilab/Singly_HB_AU (<https://doi.org/10.5281/zenodo.5099558>)⁸⁴. The DNA m^6A sites (Fig. 6f) used in this study were reported in a prior study⁹. See Supplementary Table 5 of the cited paper (<https://www.nature.com/articles/nature17640#Sec26>). Source data for Figs. 2d, 4g, and 6a, c, e and Supplementary Figs. 2c, 4b, 6d, 7c, d, f, 8c, d, 9b, c, 10b, and 11a–d are provided with this paper.

Code availability

In-house Python scripts used to perform CEST fitting, kinetic simulations, and predictions (duplex hybridization, TAR conformational transitions, and genome-wide DNA hybridization prediction) are provided at https://github.com/alhashimilab/m6A_hybridization_kinetics (<https://doi.org/10.5281/zenodo.5099562>)⁸².

Received: 6 January 2021; Accepted: 21 July 2021;

Published online: 31 August 2021

References

1. Meyer, K. D. et al. Comprehensive analysis of mRNA methylation reveals enrichment in 3' UTRs and near stop codons. *Cell* **149**, 1635–1646 (2012).
2. Dominissini, D. et al. Topology of the human and mouse m6A RNA methylomes revealed by m6A-seq. *Nature* **485**, 201–206 (2012).
3. Fu, Y., Dominissini, D., Rechavi, G. & He, C. Gene expression regulation mediated through reversible m(6)A RNA methylation. *Nat. Rev. Genet.* **15**, 293–306, (2014).
4. Roundtree, I. A., Evans, M. E., Pan, T. & He, C. Dynamic RNA modifications in gene expression regulation. *Cell* **169**, 1187–1200 (2017).
5. Zaccara, S., Ries, R. J. & Jaffrey, S. R. Reading, writing and erasing mRNA methylation. *Nat. Rev. Mol. Cell Biol.* **20**, 608–624 (2019).
6. Vanyushin, B. F., Belozersky, A. N., Kokurina, N. A. & Kadirova, D. X. 5-methylcytosine and 6-methylamino-purine in bacterial DNA. *Nature* **218**, 1066–1067, (1968).
7. Douvlataniotis, K., Bensberg, M., Lentini, A., Gylemo, B. & Nestor, C. E. No evidence for DNA N(6)-methyladenine in mammals. *Sci. Adv.* **6**, eaay3335 (2020).
8. Li, Z. et al. N(6)-methyladenine in DNA antagonizes SATB1 in early development. *Nature* **583**, 625–630 (2020).
9. Wu, T. P. et al. DNA methylation on N(6)-adenine in mammalian embryonic stem cells. *Nature* **532**, 329–333 (2016).
10. Liu, N. et al. N(6)-methyladenosine-dependent RNA structural switches regulate RNA-protein interactions. *Nature* **518**, 560–564 (2015).
11. Huang, L., Ashraf, S., Wang, J. & Lilley, D. M. Control of box C/D snoRNP assembly by N6-methylation of adenine. *EMBO Rep.* **18**, 1631–1645 (2017).
12. Roost, C. et al. Structure and thermodynamics of N6-methyladenosine in RNA: a spring-loaded base modification. *J. Am. Chem. Soc.* **137**, 2107–2115 (2015).
13. Choi, J. et al. N(6)-methyladenosine in mRNA disrupts tRNA selection and translation-elongation dynamics. *Nat. Struct. Mol. Biol.* **23**, 110–115 (2016).
14. Slobodin, B. et al. Transcription Impacts the Efficiency of mRNA Translation via Co-transcriptional N6-adenosine Methylation. *Cell* **169**, 326–337.e312 (2017).
15. Louloui, A., Ntini, E., Conrad, T. & Orom, U. A. V. Transient N-6-methyladenosine transcriptome sequencing reveals a regulatory role of m6A in splicing efficiency. *Cell Rep.* **23**, 3429–3437 (2018).

16. Du, K. et al. Epigenetically modified N(6)-methyladenine inhibits DNA replication by human DNA polymerase ϵ . *DNA Repair* **78**, 81–90 (2019).
17. Aschenbrenner, J. et al. Engineering of a DNA polymerase for direct m(6) A sequencing. *Angew. Chem. Int. Ed. Engl.* **57**, 417–421 (2018).
18. Rangadurai, A., Szymanski, E. S., Kimsey, I. J., Shi, H. & Al-Hashimi, H. M. Characterizing micro-to-millisecond chemical exchange in nucleic acids using off-resonance R1rho relaxation dispersion. *Prog. Nucl. Magn. Reson. Spectrosc.* **112–113**, 55–102 (2019).
19. Palmer, A. G. 3rd & Massi, F. Characterization of the dynamics of biomacromolecules using rotating-frame spin relaxation NMR spectroscopy. *Chem. Rev.* **106**, 1700–1719 (2006).
20. Palmer, A. G. 3rd Chemical exchange in biomacromolecules: past, present, and future. *J. Magn. Reson.* **241**, 3–1 (2014).
21. Shi, H. et al. NMR chemical exchange measurements reveal that N(6)-methyladenosine slows RNA annealing. *J. Am. Chem. Soc.* **141**, 19988–19993 (2019).
22. Cisse, I. I., Kim, H. & Ha, T. A rule of seven in Watson-Crick base-pairing of mismatched sequences. *Nat. Struct. Mol. Biol.* **19**, 623–627 (2012).
23. Xu, S. C. et al. Real-time reliable determination of binding kinetics of DNA hybridization using a multi-channel graphene biosensor. *Nat. Commun.* **8**, 14902 (2017).
24. Tawa, K. & Knoll, W. Mismatching base-pair dependence of the kinetics of DNA-DNA hybridization studied by surface plasmon fluorescence spectroscopy. *Nucleic Acids Res.* **32**, 2372–2377 (2004).
25. Engel, J. D. & von Hippel, P. H. Effects of methylation on the stability of nucleic acid conformations: studies at the monomer level. *Biochemistry* **13**, 4143–4158 (1974).
26. Engel, J. D. & von Hippel, P. H. Effects of methylation on the stability of nucleic acid conformations. Studies at the polymer level. *J. Biol. Chem.* **253**, 927–934 (1978).
27. Hammes, G. G., Chang, Y. C. & Oas, T. G. Conformational selection or induced fit: a flux description of reaction mechanism. *Proc. Natl Acad. Sci. USA* **106**, 13737–13741 (2009).
28. Sekhar, A. et al. Conserved conformational selection mechanism of Hsp70 chaperone-substrate interactions. *Elife* **7**, <https://doi.org/10.7554/eLife.32764> (2018).
29. Zhao, B., Hansen, A. L. & Zhang, Q. Characterizing slow chemical exchange in nucleic acids by carbon CEST and low spin-lock field R(1rho) NMR spectroscopy. *J. Am. Chem. Soc.* **136**, 20–23 (2014).
30. Vallurupalli, P., Bouvignies, G. & Kay, L. E. Studying “invisible” excited protein states in slow exchange with a major state conformation. *J. Am. Chem. Soc.* **134**, 8148–8161 (2012).
31. Bouvignies, G. & Kay, L. E. A 2D (1)(3)C-CEST experiment for studying slowly exchanging protein systems using methyl probes: an application to protein folding. *J. Biomol. NMR* **53**, 303–310 (2012).
32. McConnell, H. M. Reaction rates by nuclear magnetic resonance. *J. Chem. Phys.* **28**, 430–431 (1958).
33. Mulder, F. A., Mittermaier, A., Hon, B., Dahlquist, F. W. & Kay, L. E. Studying excited states of proteins by NMR spectroscopy. *Nat. Struct. Biol.* **8**, 932–935 (2001).
34. Kimsey, I. J., Petzold, K., Sathyamoorthy, B., Stein, Z. W. & Al-Hashimi, H. M. Visualizing transient Watson-Crick-like mispairs in DNA and RNA duplexes. *Nature* **519**, 315–320 (2015).
35. Abramov, G., Velyvis, A., Rennella, E., Wong, L. E. & Kay, L. E. A methyl-TROSY approach for NMR studies of high-molecular-weight DNA with application to the nucleosome core particle. *Proc. Natl Acad. Sci. USA* **117**, 12836–12846 (2020).
36. Liu, B. et al. A potentially abundant junctional RNA motif stabilized by m(6)A and Mg(2). *Nat. Commun.* **9**, 2761 (2018).
37. Koss, H., Rance, M. & Palmer, A. G. 3rd General expressions for R1rho relaxation for N-site chemical exchange and the special case of linear chains. *J. Magn. Reson.* **274**, 36–45 (2017).
38. Bhaswati Goswami, B. L. G. & Jones, R. A. Nitrogen-15-labeled oligodeoxynucleotides. 5. Use of 15N NMR to probe H-bonding in an O6MeG-T base pair. *J. Am. Chem. Soc.* **115**, 3832–3833 (1993).
39. Van Charldorp, R., Heus, H. A. & Van Knippenberg, P. H. Adenosine dimethylation of 16S ribosomal RNA: effect of the methyl groups on local conformational stability as deduced from electrophoretic mobility of RNA fragments in denaturing polyacrylamide gels. *Nucleic Acids Res.* **9**, 267–275 (1981).
40. Aboul-ela, F., Koh, D., Tinoco, I. Jr. & Martin, F. H. Base-base mismatches. Thermodynamics of double helix formation for dCA3XA3G + dCT3YT3G (X, Y = A,C,G,T). *Nucleic Acids Res.* **13**, 4811–4824 (1985).
41. Bannwarth, S. & Gatignol, A. HIV-1 TAR RNA: the target of molecular interactions between the virus and its host. *Curr. HIV Res.* **3**, 61–71 (2005).
42. Dethoff, E. A., Petzold, K., Chugh, J., Casiano-Negroni, A. & Al-Hashimi, H. M. Visualizing transient low-populated structures of RNA. *Nature* **491**, 724–728 (2012).
43. Chu, C. C., Plangger, R., Kreutz, C. & Al-Hashimi, H. M. Dynamic ensemble of HIV-1 RRE stem IIB reveals non-native conformations that disrupt the Rev-binding site. *Nucleic Acids Res.* **47**, 7105–7117 (2019).
44. Bisaria, N., Greenfeld, M., Limouse, C., Mabuchi, H. & Herschlag, D. Quantitative tests of a reconstitution model for RNA folding thermodynamics and kinetics. *Proc. Natl Acad. Sci. USA* **114**, E7688–E7696 (2017).
45. Zhang, J. X. et al. Predicting DNA hybridization kinetics from sequence. *Nat. Chem.* **10**, 91–98 (2018).
46. Abakir, A. et al. N(6)-methyladenosine regulates the stability of RNA:DNA hybrids in human cells. *Nat. Genet.* **52**, 48–55 (2020).
47. Konno, M. et al. Distinct methylation levels of mature microRNAs in gastrointestinal cancers. *Nat. Commun.* **10**, 3888 (2019).
48. Decatur, W. A. & Fournier, M. J. RNA-guided nucleotide modification of ribosomal and other RNAs. *J. Biol. Chem.* **278**, 695–698 (2003).
49. Seraphin, B., Kretzner, L. & Rosbash, M. A U1 snRNA-pre-mRNA base pairing interaction is required early in yeast spliceosome assembly but does not uniquely define the 5' cleavage site. *EMBO J.* **7**, 2533–2538 (1988).
50. Will, C. L. & Luhrmann, R. Spliceosome structure and function. *Cold Spring Harb. Perspect Biol.* **3**, <https://doi.org/10.1101/cshperspect.a003707> (2011).
51. Klinge, S. & Woolford, J. L. Jr. Ribosome assembly coming into focus. *Nat. Rev. Mol. Cell Biol.* **20**, 116–131 (2019).
52. Kierzek, E. & Kierzek, R. The thermodynamic stability of RNA duplexes and hairpins containing N6-alkyladenosines and 2-methylthio-N6-alkyladenosines. *Nucleic Acids Res.* **31**, 4472–4480 (2003).
53. Xu, C. C. et al. Structural basis for selective binding of m6A RNA by the YTHDC1 YTH domain. *Nat. Chem. Biol.* **10**, 927–929 (2014).
54. Zimmer, D. P. & Crothers, D. M. NMR of enzymatically synthesized uniformly 13C15N-labeled DNA oligonucleotides. *Proc. Natl Acad. Sci. USA* **92**, 3091–3095 (1995).
55. Delaglio, F. et al. NMRPipe: a multidimensional spectral processing system based on UNIX pipes. *J. Biomol. NMR* **6**, 277–293 (1995).
56. Nikolova, E. N., Gottardo, F. L. & Al-Hashimi, H. M. Probing transient Hoogsteen hydrogen bonds in canonical duplex DNA using NMR relaxation dispersion and single-atom substitution. *J. Am. Chem. Soc.* **134**, 3667–3670 (2012).
57. Nikolova, E. N. et al. Transient Hoogsteen base pairs in canonical duplex DNA. *Nature* **470**, 498–502 (2011).
58. Hansen, A. L., Nikolova, E. N., Casiano-Negroni, A. & Al-Hashimi, H. M. Extending the range of microsecond-to-millisecond chemical exchange detected in labeled and unlabeled nucleic acids by selective carbon R(1rho) NMR spectroscopy. *J. Am. Chem. Soc.* **131**, 3818–3819 (2009).
59. Bothe, J. R., Stein, Z. W. & Al-Hashimi, H. M. Evaluating the uncertainty in exchange parameters determined from off-resonance R1rho relaxation dispersion for systems in fast exchange. *J. Magn. Reson.* **244**, 18–29 (2014).
60. Abou Assi, H. et al. 2'-O-Methylation can increase the abundance and lifetime of alternative RNA conformational states. *Nucleic Acids Res.* <https://doi.org/10.1093/nar/gkaa928> (2020).
61. Rangadurai, A., Shi, H. & Al-Hashimi, H. M. Extending the sensitivity of CEST NMR spectroscopy to micro-to-millisecond dynamics in nucleic acids using high-power radio-frequency fields. *Angew. Chem. Int. Ed. Engl.* **59**, 11262–11266 (2020).
62. Vallurupalli, P., Sekhar, A., Yuwen, T. & Kay, L. E. Probing conformational dynamics in biomolecules via chemical exchange saturation transfer: a primer. *J. Biomol. NMR* **67**, 243–271 (2017).
63. Yuwen, T. & Kay, L. E. Longitudinal relaxation optimized amide (1)H-CEST experiments for studying slow chemical exchange processes in fully protonated proteins. *J. Biomol. NMR* **67**, 295–307 (2017).
64. Yanjiao Wang, G. H., Jiang, X., Yuwen, T. & Xue, Y. Chemical shift prediction of RNA imino groups: application toward characterizing RNA excited states. *Nat. Commun.* **12**, 1595 (2021).
65. Gueron, M., Kochoyan, M. & Leroy, J. L. A single mode of DNA base-pair opening drives imino proton exchange. *Nature* **328**, 89–92 (1987).
66. Szulik, M. W., Voehler, M. & Stone, M. P. NMR analysis of base-pair opening kinetics in DNA. *Curr. Protoc. Nucleic Acid Chem.* **59**, 7.20.21–18 (2014).
67. Sorgenfrei, S. et al. Label-free single-molecule detection of DNA-hybridization kinetics with a carbon nanotube field-effect transistor. *Nat. Nanotechnol.* **6**, 126–132 (2011).
68. Wallace, M. I., Ying, L., Balasubramanian, S. & Klenerman, D. Non-Arrhenius kinetics for the loop closure of a DNA hairpin. *Proc. Natl Acad. Sci. USA* **98**, 5584–5589 (2001).
69. Bloomfield, V. A. et al. *Nucleic Acids: Structure, Properties, and Functions* (University Science Books, 2000).
70. Lu, X. J. & Olson, W. K. 3DNA: a software package for the analysis, rebuilding and visualization of three-dimensional nucleic acid structures. *Nucleic Acids Res.* **31**, 5108–5121 (2003).
71. Rangadurai, A. et al. Why are Hoogsteen base pairs energetically disfavored in A-RNA compared to B-DNA? *Nucleic Acids Res.* **46**, 11099–11114 (2018).

72. Aduri, R. et al. AMBER force field parameters for the naturally occurring modified nucleosides in RNA. *J. Chem. Theory Comput.* **3**, 1464–1475 (2007).
73. Swails, J., Zhu, T., He, X. & Case, D. A. AFNMR: automated fragmentation quantum mechanical calculation of NMR chemical shifts for biomolecules. *J. Biomol. NMR* **63**, 125–139 (2015).
74. Shi, H. et al. Rapid and accurate determination of atomistic RNA dynamic ensemble models using NMR and structure prediction. *Nat. Commun.* **11**, 5531 (2020).
75. Richardson, W. H., Peng, C., Bashford, D., Noodleman, L. & Case, D. A. Incorporating solvation effects into density functional theory: calculation of absolute acidities. *Int. J. Quantum Chem.* **61**, 207–217 (1997).
76. Orlovsky, N. I., Al-Hashimi, H. M. & Oas, T. G. Exposing hidden high-affinity RNA conformational states. *J. Am. Chem. Soc.* **142**, 907–921 (2020).
77. Meagher, N. E. & Rorabacher, D. B. Mathematical treatment for very rapid 2nd-order reversible kinetics as measured by stopped-flow spectrophotometry with corrections for the cell concentration gradient. *J. Phys. Chem.* **98**, 12590–12593 (1994).
78. Guo, Q., Lu, M. & Kallenbach, N. R. Effect of hemimethylation and methylation of adenine on the structure and stability of model DNA duplexes. *Biochemistry* **34**, 16359–16364 (1995).
79. Berman, H. M. et al. The Protein Data Bank. *Nucleic Acids Res.* **28**, 235–242 (2000).
80. Lu, X. J., Bussemaker, H. J. & Olson, W. K. DSSR: an integrated software tool for dissecting the spatial structure of RNA. *Nucleic Acids Res.* **43**, e142 (2015).
81. Leontis, N. B. & Westhof, E. Geometric nomenclature and classification of RNA base pairs. *RNA* **7**, 499–512 (2001).
82. Liu, B. et al. A quantitative model predicts how m6A reshapes the kinetic landscape of nucleic acid hybridization and conformational transitions. *Beilstein J. Org. Chem.* **17**, 125 (2021). <https://doi.org/10.5281/zenodo.5106694> (2021).
83. Liu, B. et al. A quantitative model predicts how m6A reshapes the kinetic landscape of nucleic acid hybridization and conformational transitions. *alhashimilab/m6A_ES* <https://doi.org/10.5281/zenodo.5099581> (2021).
84. Liu, B. et al. A quantitative model predicts how m6A reshapes the kinetic landscape of nucleic acid hybridization and conformational transitions. *Beilstein J. Org. Chem.* **17**, 125 (2021). <https://doi.org/10.5281/zenodo.5099558> (2021).

Acknowledgements

We thank members of the Al-Hashimi laboratory for their assistance and critical comments on the manuscript. We would like to thank Yanjiao Wang and Prof. Xue Yi (Tsinghua University) for the help with the ^1H CEST experiment, Prof. Terrence Oas (Duke University) for advice about kinetic simulations and calculations, and Prof. Qi Zhang for providing the 2D [^{13}C , ^1H] CEST pulse sequence based on which the methyl CEST sequence was derived. This work was supported by the US National Institute for General Medical Sciences (1R01GM132899) and US National Institute of Health (R01GM089846) to H.M.A., the Austrian Science Fund (FWF, project P30370 and P32773) and the Austrian Research Promotion Agency FFG (West Austrian BioNMR, 858017) to C.K. and the National Institute for Allergy and Infectious Diseases (U54 AI150470) to D.A.C.

Author contributions

B.L. and H.M.A. conceived the project and experimental design. B.L. prepared NMR samples, performed NMR experiments, and analyzed NMR data with the help from H.S., A.R. and C.-C.C., F.N., K.A.E. and C.K. prepared ($^{13}\text{CH}_3$)-m⁶A RNA phosphoramidite and $^{13}\text{C}_8$, $^{13}\text{C}_2$ -labeled m⁶dA phosphoramidite. B.L. performed kinetic simulations and predictions. H.S. performed proton CEST and imino proton exchange experiments. A.R. performed MD simulations. H.S. and D.A.C. performed Automated fragmentation quantum mechanics/molecular mechanics (AF-QM/MM) chemical-shift calculations. B.L. and H.S. performed the PDB survey. H.M.A. and B.L. wrote the manuscript with critical input from H.S. and A.R.

Competing interests

H.M.A. is an advisor to and holds an ownership interest in Nymirum, an RNA-based drug discovery company. C.K. is an advisor to and holds an ownership interest in INNotope, a company providing RNA stable isotope labeling products. The remaining authors declare no competing interests.

Additional information

Supplementary information The online version contains supplementary material available at <https://doi.org/10.1038/s41467-021-25253-8>.

Correspondence and requests for materials should be addressed to H.M.A.-H.

Peer review information *Nature Communications* thanks Joseph Puglisi and other, anonymous, reviewers for their contributions to the peer review of this work. Peer review reports are available.

Reprints and permission information is available at <http://www.nature.com/reprints>

Publisher's note Springer Nature remains neutral with regard to jurisdictional claims in published maps and institutional affiliations.



Open Access This article is licensed under a Creative Commons Attribution 4.0 International License, which permits use, sharing, adaptation, distribution and reproduction in any medium or format, as long as you give appropriate credit to the original author(s) and the source, provide a link to the Creative Commons license, and indicate if changes were made. The images or other third party material in this article are included in the article's Creative Commons license, unless indicated otherwise in a credit line to the material. If material is not included in the article's Creative Commons license and your intended use is not permitted by statutory regulation or exceeds the permitted use, you will need to obtain permission directly from the copyright holder. To view a copy of this license, visit <http://creativecommons.org/licenses/by/4.0/>.

© The Author(s) 2021